Contents lists available at ScienceDirect

Energy Conversion and Management

journal homepage: www.elsevier.com/locate/enconman

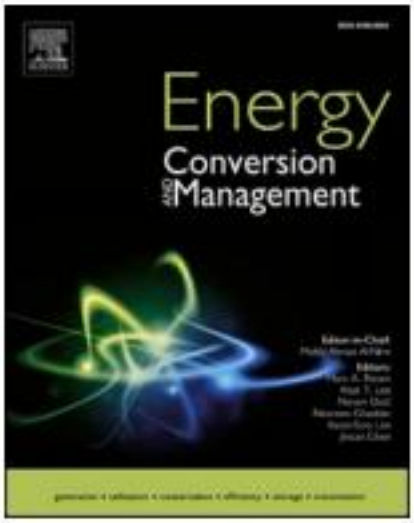

Research Paper

Sustainable flare gas valorization using an optimized novel hybrid solid oxide fuel cell and micro gas turbine system with integrated absorption-based carbon capture

Mostafa Mahboobi a,b,* , Antoine Verhaeghe o, Ward De Paepe b,d,e

- a Department of Mechanical Engineering, University of Kashan, Kashan, Iran
- b Thermal Engineering and Combustion Unit, University of Mons, Mons, Belgium
- c Chemical and Biochemical Process Engineering Unit, University of Mons, Mons, Belgium
- d Umons Micro gAsturbine Research Centre UMARC, Mons, Belgium
- e Wel Research Institute, Avenue Pasteur, 6 1300 Wavre, Belgium

ARTICLE INFO

Keywords: Flare gas recovery

Solid oxide fuel cell Micro gas turbine Carbon capture

Gas sweetening

Waste-to-energy

ABSTRACT Flaring associated gas leads to significant energy losses and greenhouse gas emissions. While recovery improves resource use and reduces environmental impact, direct use in gas turbines and solid oxide fuel cells (SOFCs) still emits CO2, making carbon capture essential. This study develops a detailed Aspen Plus model of a hybrid micro gas turbine (mGT) and SOFC system, integrated with a flare gas sweetening unit (GSU) and carbon capture (CC). An exhaust gas recirculation (EGR) configuration is also examined to boost CO2 concentration for improved capture. Each subsystem was validated prior to integration. The GSU achieved a minimal reboiler duty with a 30 m absorber and a solvent flow of 0.29 kg/s, meeting the H2S removal standards. For the SOFC, the optimal values for current density, steam-to-carbon ratio, and fuel utilization factor were 178 mA/cm2, 2.5, and 0.85, respectively. The hybrid mGT + SOFC achieved electrical and exergy efficiencies of 68.7% and 66.1%. The CC unit utilized waste heat from SOFC and mGT exhausts to partially supply reboiler duty. Meanwhile, a stripper pressure of 1.8 bar, a 14 m absorber, and L/G ratios of 1.0 (without EGR) and 2.4 (with EGR at 0.67) minimized energy demand. The mGT + SOFC configuration delivered the best performance, with a carbon intensity of 288.5 gCO2/kWhe (without CC) and ∼30.5 gCO2/kWhe (with CC), indicating a reduction of ∼89% in CO2. Overall, the proposed hybrid system offers an efficient pathway for flare gas valorization, achieving high efficiency and significantly lower CO2 emissions.

1. Introduction

In the last decades, industrialization and population growth have created an enormous worldwide demand for energy. The majority of this demand is still met by fossil fuels, whose extensive use, apart from having a limited supply, also has severe environmental consequences in the form of high greenhouse gas emissions and global warming. Furthermore, economic limitations and international regulations aimed at reducing pollutants have underscored the need for the application of new technologies in energy systems. The effective utilization of existing resources and the recovery of wasted energy streams, such as flare gas, have become essential strategies for increasing energy efficiency and reducing environmental impacts in this regard. Flare gas is the associated natural gas of crude oil that, due to the lack of appropriate

collection or recycling infrastructure, is burned in a controlled manner in most oil and gas fields. This practice, aside from wasting potential energy, is a considerable source of atmospheric pollutant emissions [1]. Globally, gas flaring resulted in the emission of approximately 400 million tons of CO2, equivalent to some 1.5% of the total greenhouse gas emissions across the globe, which is roughly one-third of Europe′s natural gas consumption [2] Besides its impact on the environment, flaring is also a big loss of energy because the estimated 140 billion cubic meters of gas which are annually flared equates to about 750 billion kWh of electricity, a sum greater than the whole of the African continent′ s annual electricity consumption [3]. Having observed both the energy and environmental aspects of this issue, further global commitment was evidenced in the form of the Zero Routine Flaring by 2030 initiative undertaken in 2015 by the World Bank and the United Nations to completely eliminate routine flaring by 2030 with the support of

* Corresponding author at: Department of Mechanical Engineering, University of Kashan, Kashan, Iran. E-mail address: mahboobi@grad.kashanu.ac.ir (M. Mahboobi).

	Nomenclature	S/C	Steam-to-carbon ratio
		SRD	Specific Reboiler Duty, MJ/kgCO2
Acronyms		T	Temperature, ◦ C
CC	Carbon Capture	Uf	Fuel utilization factor
DEA	Diethanolamine	V	Cell voltage, mV
EGR	Exhaust Gas Recirculation	$\dot{V}$	flow rate, m3/s
GSU	Gas Sweetening Unit	$\dot{W}$	Electrical power, kWe
MEA	Monoethanolamine		
mGT	micro Gas Turbine	Greek Symbols	
SOFC	Solid Oxide Fuel Cell	ΔVanode	Effect of fuel composition on cell voltage, mV

	Nomenclature	S/C	Steam-to-carbon ratio
TIT	Turbine Inlet Temperature	ΔVcathode	Effect of oxidant composition on cell voltage, mV
		ΔVP	Effect of operating pressure on cell voltage, mV
Symbols		ΔVT	Effect of operating temperature and current density on cell
A	Active area, m2		voltage, mV
$\dot{Ex}$	Exergy, kW	η	efficiency, %
ex	Specific exergy, kJ/kg		
F	Faraday constant, C/mol	Subscripts	
Ic	Current density, mA/cm2	aux	auxiliary
L/G	Liquid-to-gas ratio, kg/kg	ch	chemical
LHV	Lower Heating Value, kJ/kg	el	electrical
$\dot{m}$	mass flow rate, kg/s	l	loss
		ph	physical
n	mole flow rate, mol/h	ref	reference
P	pressure, kPa	sg	sweet gas
Q	heat transfer, kJ		
$\dot{Q}$	Thermal power, kWth		

governments, oil producers, and development institutions [4]. These figures underscore the urgent need for effective flare gas recovery measures to mitigate both environmental and economic impacts [5,6].

According to various studies, the main methods for flare gas recovery include Gas to Power, Gas Reinjection, Gas to Liquid (GTL), Compressed Natural Gas (CNG), Syngas production, Liquefied Natural Gas (LNG), and hydrogen production [7]. Studies have shown that Gas to Power is an effective and economically viable approach to flare gas utilization, particularly in regions with limited access to the electricity grid, providing a sustainable solution for energy recovery [8].

One particularly effective strategy for utilizing flare gas is on-site power generation via distributed energy units, especially small micro gas turbine (mGT). Such units are valuable because they can convert waste gas into electricity right where the flare occurs, reducing losses from transportation, improving reliability, and significantly cutting CO2 emissions. Based on existing reviews, the application of micro gas turbines for flare gas recovery has been limited, with only a few studies addressing this area. In addition to micro gas turbines, solid oxide fuel cells (SOFCs) have emerged as a promising technology for utilizing flare gas. These fuel cells achieve direct conversion of chemical energy into electrical energy with high efficiency, effectively transforming associated gas into electrical power. Research has indicated that the application of SOFCs in flare gas systems not only produces additional electricity but also reduces greenhouse gas emissions [9]. Economic assessments have shown that employing SOFCs for flare gas recovery incurs lower costs compared to other technologies, such as conventional gas turbines [10]. Therefore, the following section focuses on studies that applied solid oxide fuel cells for flare gas recovery.

According to the work of Saidi et al. [11], the use of SOFCs at the Asalouyeh gas processing plant in Iran was simulated. In this model, sweetened flare gas was directly fed into the SOFC, with the required steam supplied through anode gas recycling. The results indicated that the system could generate about 1200 MW of electricity. Moreover, greenhouse gas emissions were reduced dramatically, from 1700 to 68 kg/s. Parametric analysis further revealed that increasing operating temperature and fuel utilization ratio, along with decreasing anode recycle ratio, significantly improved system performance and electrical efficiency. Al-khori et al. [10] investigated the integration of SOFCs with flare gas streams in offshore and onshore plants. By feeding a significant portion of the purge gas to the SOFC unit, the system could generate electricity while simultaneously eliminating emissions. The results indicated that, in the onshore example, the utilization of approximately 3.5 million stan-

dard cubic feet of gas enabled the generation of nearly 20 MW of power, and reduced CO2-equivalent emissions from 263 to 101 tons per day. In the offshore example, the injection of approximately 105,000 standard cubic feet of gas generated approximately 600 kW of power and reduced emissions from 9 to 3 tons per day. Al Jabri et al. [12] proposed an alternative approach for flare gas to power conversion using a SOFC model developed in Aspen Plus. The model incorporated existing unit operation modules such as a mixer, cooler, reactor, and heat exchanger, and was validated against published literature data. The study focused on analyzing the influence of key operating parameters, including temperature, pressure, and fuel utilization factor, on system performance. Results showed that the system achieved an overall cell electrical voltage of 818 mV at an operating temperature of 1050 ◦ C and a fuel utilization factor of 0.85. In another study by Bargo [13], a SOFC combined heat and power (CHP) system was designed to recover flare gas with high CO2 content (approximately 30%) from the Neem-Field in Western Sudan. The simulation results indicated that the system could generate 1 MW of electrical power and 0.068 MW of thermal energy, achieving an overall efficiency of 43.3% (based on LHV). Exergy analysis revealed that 38% of system losses occurred in the air preheaters. By utilizing the flared gas instead of conventional burning, the system reduced equivalent CO2 greenhouse gas emissions by 80%. According to the work of Nezhadfard [14], the SOFC + gas turbine configuration was one of the options examined. The study generally noted that integrating an SOFC with a gas turbine could be a promising option for flare gas recovery, particularly in terms of improving efficiency and reducing emissions. The major constraint mentioned was the need for further study to enhance performance, reduce costs, and test operation under real circumstances. This indicates the immense potential of SOFC for flare gas applications and also highlights the constraints for its widespread usage.

For the safe and efficient utilization of flare gas in sensitive

equipment such as mGTs and SOFCs, gas pre-treatment is essential. Chemical solvents are among the most commonly used methods for purifying natural gas, accounting for more than 95% of the techniques employed. [15]. Jafari et al. [16] demonstrated that integrating a membrane-based sweetening unit significantly improved the quality of flare gas for the GTL process. The membrane efficiently removed acid gases, yielding a purified feed that enhanced the stability and performance of downstream units such as the reformer and Fischer–Tropsch synthesis. Although this step increased electricity use by about 47% compared to the standard process, it reduced total energy demand by nearly 26%, CO2 emissions by 23%, and liquid fuel production costs by around 12%. In the study by Dinani et al. [17], flare gas recovery was modeled using a sweetening unit to remove CO2 and H2S prior to downstream use. This step ensured the gas met quality standards for reinjection or conversion. The study concluded that sweetening and NGL recovery significantly decreased emissions (above 6 million tons CO2/ year) and maintained the system' s profitability on a highly economical basis, with an NPV of $1.5 billion and a payback time of 1.6 years. Kumar et al. [18] proposed a thermo-economic model for flare gas recovery by integrating concentrated solar power with an oxy-fuel combustion cycle to co-produce electricity and clean water. Although focused on efficiency and solar integration, it assumed that flare gas must be pretreated in a sweetening unit to remove acid gases before entering the combustion chamber. Considering this step, the system achieved up to 26% higher efficiency, 33% lower fuel use, and reduced emissions compared to conventional recovery methods, underscoring the importance of feed purification via a gas sweetening unit (GSU).

Exhaust Gas Recirculation (EGR) redirects a portion of exhaust gas back into the intake, effectively lowering combustion temperature and reducing NOx emissions, thereby enhancing emission control performance [19]. In a 2025 study by Thielens et al. [20], the effect of an external EGR loop in an MTT EnerTwin® micro gas turbine was investigated. The system was modified to allow exhaust gases to be recirculated into the combustion chamber up to the point of flame extinction. Results showed that EGR increased CO2 concentration in the exhaust gases by up to 7.9%, reduced NOx emissions, and slightly improved combined heat and power production. However, higher gas recirculation rates also increased CO concentrations, creating limitations before the flame extinction point was reached. The study demonstrates the potential of EGR as a method for enhancing carbon capture in micro gas turbines. In a study by De Paepe et al [21], the impact of using EGR in a humidified micro gas turbine cycle was investigated. Simulation results showed that EGR can improve the system' s efficiency by reducing energy consumption in the carbon capture process and increasing the CO2 concentration in the exhaust gases. Additionally, combining EGR with humidification can support cleaner and more efficient power generation. This study highlights the potential of EGR in humidified micro gas turbines for producing low-carbon electricity.

Carbon Capture, Utilization, and Storage (CCUS) has emerged as a key strategy for reducing greenhouse gas

emissions and facilitating the transition toward low-carbon energy systems. It involves separating CO2 from industrial and power generation sources and storing it to prevent its release into the atmosphere, with projections indicating that CCUS could contribute up to 13% of global emission reductions by 2050. In parallel, CCUS enables the conversion of captured CO2 into valuable products, providing both environmental and economic benefits [22]. Among available technologies, post-combustion capture using aminebased absorption is one of the most mature and widely applied methods, particularly in fossil fuel and natural gas power systems [23]. Monoethanolamine (MEA) stands as the standard solvent due to its strong reactivity with CO2, well-established thermodynamic behavior, and relatively low cost [24]. Furthermore, integration of advanced amine-based post-combustion carbon capture configurations with combined cycle gas turbines can significantly reduce the efficiency penalty, achieving up to a 30% improvement in net power output compared to conventional configurations [25]. In the study by

Snytnikov and Potemkin [26] a carbon capture unit was integrated with a low-temperature steam reforming process for flare gas, enabling CO2 separation and reinjection into oil reservoirs. This approach was shown to both enhance oil recovery and reduce atmospheric CO2 emissions, while allowing the captured CO2 to be utilized as emission quotas for "blue" hydrogen production in sites where carbon capture is infeasible. Verhaeghe et al. [27] demonstrated that solvent selection plays a crucial role in reducing the energy penalty of amine-based carbon capture in micro gas turbine systems. Their results showed that replacing conventional MEA with a blended methyldiethanolamine/piperazine (MDEA/PZ) solvent reduced the specific reboiler duty by approximately 15% and improved overall thermal and electrical performance. The study also found that advanced process configurations provided only minor improvements, confirming that solvent optimization is more effective than configuration modifications for enhancing carbon capture efficiency in low-CO2 gas turbine applications. Qian et al [28] developed a novel hybrid natural gas and coal-fired system, in which the gas turbine exhaust was directly introduced into the coal-fired boiler to improve power generation efficiency and carbon capture performance. The results showed that the power generated from the gas turbine exhaust increased by 19.90%, while the net efficiency of natural gas power generation reached 61.49%, representing an improvement of 4.09% points compared to the conventional system. Furthermore, the 2.40-fold increase in CO2 concentration in the flue gas reduced the energy consumption of the carbon capture system by 22.03%. In this study by Li and Zhang [29], a novel Selective-Exhaust Gas Recirculation (S-EGR) strategy was proposed to improve the efficiency of gas turbine combined cycle (GTCC) systems with post-combustion CO2 capture under part-load conditions. The proposed method eliminated the need for exhaust gas compression and cooling, thereby reducing energy consumption and improving overall system performance. The results showed that at 50% load, the system achieved a 90% CO2 capture rate and more than doubled the CO2 concentration in the exhaust gas, reducing the MEA capture load by 31.67%. As a result, the part-load efficiency increased by 0.93 percentage points, and the bottoming cycle power output increased by 12.57 MW, demonstrating improved thermodynamic performance. Moosazadeh et al. [30] proposed the HydraCap-FF system, integrating carbon capture with flare gas utilization for hydrogen production. The carbon capture facility separates and reinjects CO2 throughout the process, enabling improved oil recovery and reducing CO2 emissions, thereby enhancing the efficiency of the resource. A next-generation version, HydraCap-RE, also incorporates solar-thermal assistance, thereby further reducing the carbon footprint and increasing hydrogen output, while offering substantial environmental and economic advantages over conventional approaches.

Although there is growing interest in utilizing flare gas, no detailed hybrid mGT + SOFC system has been proposed. Standalone operation of mGTs or SOFCs still results in significant CO2 emissions, and conventional carbon capture solutions typically require large installations with relatively low overall efficiency. Integrating an SOFC with an mGT improves electrical efficiency, thereby enhancing the technical feasibility and effectiveness of carbon capture. The main novelties and contributions of this study are as follows:

- Development of a novel system integrating GSU, mGT, SOFC, EGR, and absorption-based carbon capture (CC) to address flare gas valorization, which has not been reported in previous studies.
- Investigation of the combined operation of SOFC and mGT to exploit their complementary characteristics, resulting in higher electrical and exergy efficiencies than either unit operating independently.
- Utilization of the high-temperature exhaust from the hybrid mGT + SOFC system to supply the carbon capture unit, reducing the energy penalty of the CC process and improving overall system performance.
- Assessment of the impact of pre-treatment and auxiliary units, including the GSU, EGR, and CC, on system

efficiency and CO2 emissions, providing insights into their optimal integration.

• Proposal of a compact system suitable for offshore or remote locations, enabling independent operation with a small footprint, maximizing energy recovery and minimizing CO2 emissions.

2. Simulation approach

This section provides an overview of each cycle and subsystem considered in this study, which are individually introduced and validated. The simulations are performed using Aspen Plus V14.0. The subsystems are presented in the following order: the gas sweetening unit, the solid oxide fuel cell, the micro gas turbine, the exhaust gas recirculation, and finally, the carbon capture. The overall schematic of the investigated hybrid system is illustrated in Fig. 1.

2.1. Gas sweetening unit

Sulfur compounds, namely H2S, in flare gas must be removed prior to fueling the SOFC system because H2S poisoning of the electrode is harmful to SOFC performance. A gas sweetening unit is, therefore, needed for flare gas to eliminate sulfur compounds before feeding it to the SOFC. The unit uses an absorption–regeneration process, where acid gases are absorbed by a solvent in the absorber and released in the regenerator for solvent recovery.

For the validation of this unit, as shown in the process flow diagram in Fig. 2, the sour flare gas characterized in Ref. [17] is introduced into the absorption column (Stream 3), while DEA (diethanolamine) with a weight concentration of 30% enters from the top of the column at a circulation rate of 29,520 kmol/h (Stream 16). DEA was selected due to its low reaction heat, enhanced acid gas absorption capacity, and reduced energy requirement, along with its potential for selective H2S removal in mixed gas streams [31]. As the two phases interact and mass transfer occurs between them, the sweet gas (sg) exits the top of the column with the specifications detailed in Table 1, and the rich amine exits from the bottom of the column (Stream 4). Subsequently, the pressure of the rich amine is reduced to 620.5 kPa before it enters the flash drum to separate any remaining hydrocarbons. Following this, it passes through a heat exchanger, where its temperature is adjusted to 84.75 ◦ C, allowing it to be introduced into the regeneration column (Stream 8). In this column, the amine regeneration takes place, with acid gases being removed from the top of the column, as indicated by the specifications in Table 1. The acid gas separated in the stripper cannot be vented directly to the atmosphere. In practice, it is usually directed to a

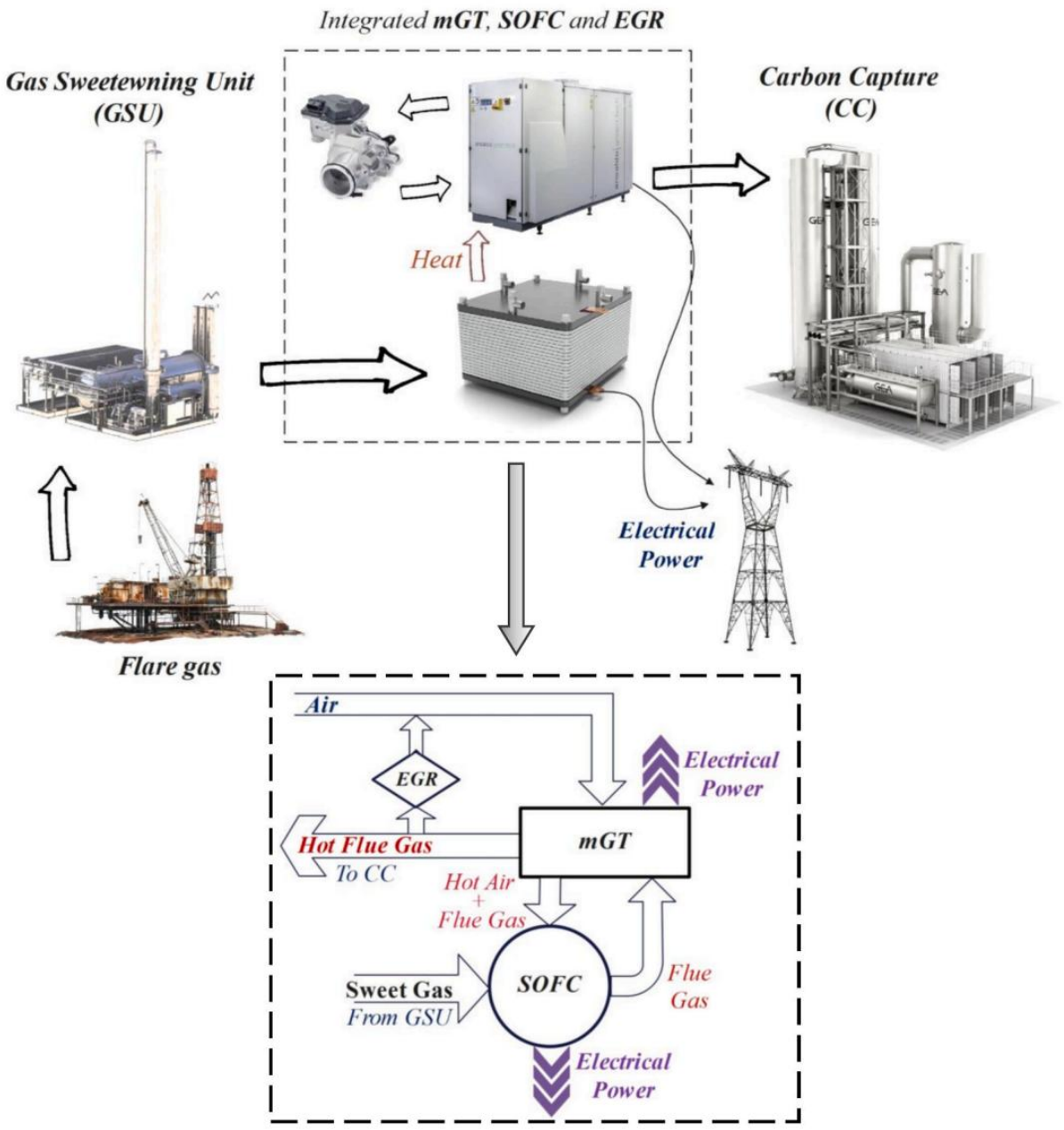

Fig. 1. Schematic of the proposed system (GSU + mGT + SOFC + EGR + CC), showing the system flow paths with arrows, with the block diagram of the hybrid system highlighted within the dashed box.

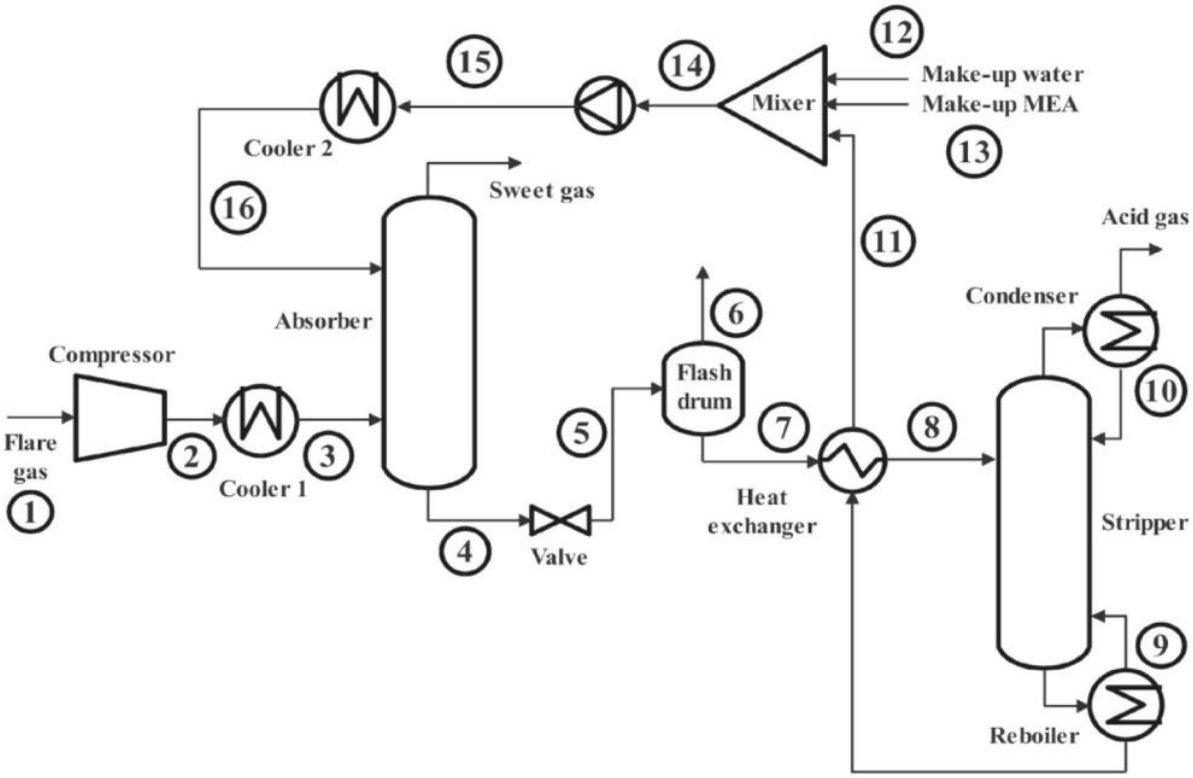

Fig. 2. Process flow diagram for the gas sweetening unit.

Table 1 Operating data, simulated results, and relative error percentage [17].

Dinani et al[17]	Simulation Data	R.E.(%)
		6.31
		0.31
0.0014	0.00136	2.87
<0.0001	0.00005739	–
		0.26
		1.61
		0.23
		0.44
		0.47
124.9	125.36	0.37
54.48	53.80	1.25
	35.4713,74064.8148.8910670.53950.3942	37.7113782.7764.6448.101064.520.54180.3961

Sulphur Recovery Unit (SRU), where it can be converted to elemental sulphur to avoid acidic emissions [32]. The lean amine exits from the bottom of the column at a pressure of 217.2 kPa. After passing through a heat exchanger, stream 14 is pressurized by the pump to the required absorption pressure (6860 kPa), and its temperature is reduced to 35 ◦ C, making it suitable for re-entry into the absorption process.

Based on Table 1, the comparison of the obtained simulation results for the gas sweetening unit with a similar plant studied by Dinani et al. [17] shows very good agreement. For this simulation, the operating parameters of the absorber and stripper columns, such as the number of stages, pressure, and temperature, and flare gas

specifications, were set according to this reference, resulting in an average relative error of 1.41%, with maximal deviation not exceeding 6.4%.

2.2. Solid oxide fuel cell

As shown in Fig. 3, the process begins with sweet gas (stream 1) entering the "Ejector" mixer block, where it combines with recycled anode gas (stream 6). This recycled stream is obtained by splitting the anode off-gas (stream 5) using the "Split" Fsplitter block. A design-spec function calculates the exact split fraction required to achieve the desired steam-to-carbon (S/C) ratio. Another design-spec determines the

necessary sweet gas pressure to drive the recycling process, based on the pressure ratio defined in Ref. [33]. The mixed fuel (stream 2) then enters the pre-reforming section. First, it passes through "Cooler 1" (a Heater block), which simulates the temperature drop caused by the endothermic reforming reactions. The cooled stream (stream 3) then feeds into the" Reformer" (Rgibbs reactor), where higher hydrocarbons and methane undergo steam reforming at equilibrium. A heat stream (Q1) connects "Cooler 1" to the" Reformer" and a design-spec ensures adiabatic operation of the "Reformer" by adjusting the outlet temperature, typically to above 500 ◦ C. The chemical reactions that occur in the "Reformer" block are [33]:

Steam reforming reactions:

$$C_nH_{2n+2} + nH_2O \Leftrightarrow (2n+1)H_2 + nCO$$

(1)

Water –gas shift reaction :

$$CO + H_2O \Leftrightarrow CO_2 + H_2$$

(2)

In the "ANODE" , three key reactions occur: 1) electrochemical oxidation of $H2$, 2) steam reforming of $CH4$, and 3) water–gas shift of CO. Although the model simplifies by assuming only H2 participates electrochemically, the equilibrium approach accurately captures the behavior due to the high-temperature conditions (large equilibrium constant for $H2$ oxidation). The reactions considered in this block are [33]:

Electrochemical reaction:

$$H_2 + \frac{1}{2}O_2 \Rightarrow H_2O$$

(3)

Methane steam reforming :

$$CH_4 + H_2O \Leftrightarrow CO + 3H_2$$

(4)

Water –gas shift reaction :

$$CO + H_2O \Leftrightarrow CO_2 + H_2$$

(5)

On the air side, inlet air (stream 9) is preheated in the "Recuperator" Heatx block by hot exhaust (stream 14). The preheated air (stream 10) enters the "Cathode" Sep block, where oxygen (stream 11) is separated for the anode reaction. A Calculator block determines the O2 flow rate ($nO2,required$) based on the equivalent hydrogen molar flow ($nH2,equivalent$) and the fuel utilization factor (Uf), as calculated according to Eq. (6). The "Heater 1" block accounts for electrochemical heating (Q3), matching the anode outlet (stream 5) and depleted air (stream 13) temperatures to prevent any temperature gradient at outlets [33].

$$n_{O_2,required} = 0.5(U_f)(n_{H_2,equivalent})$$

(6)

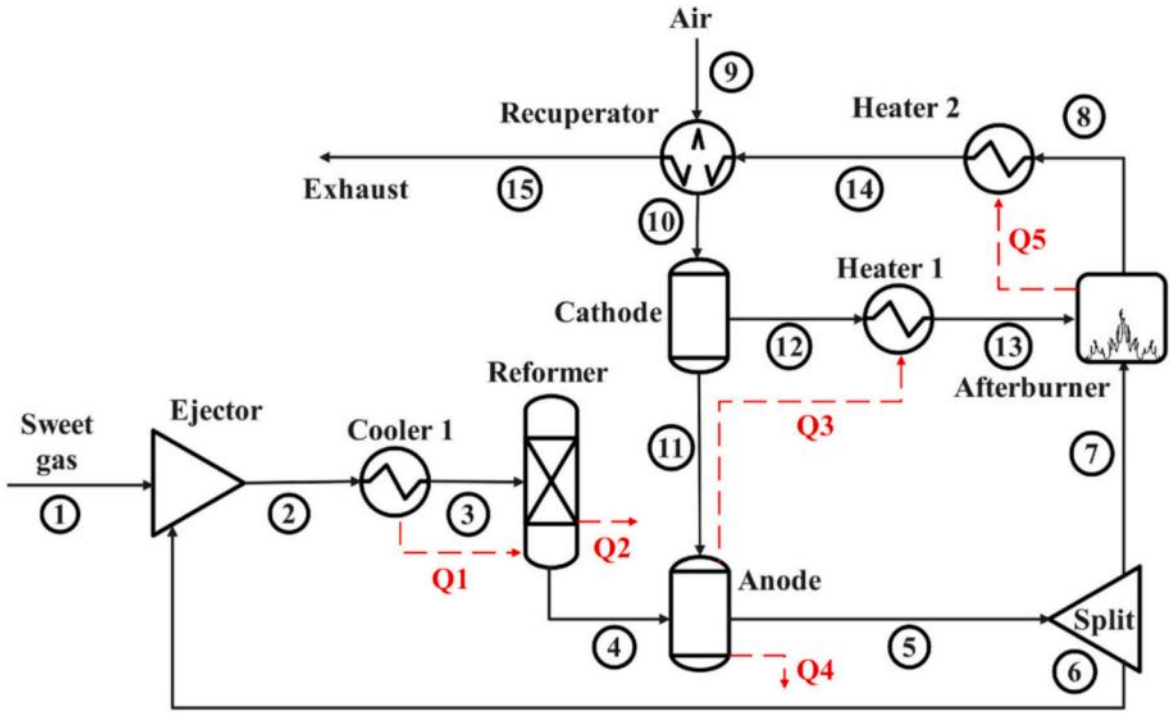

Fig. 3. Process flow diagram of SOFC, with red streams indicating heat flow from the components.

The $n_{H_2,equivalent}$ is determined as follows [33]:

$$n_{H_2,equivalent} = n_{H_2,in} + 1 \times n_{CO,in} + 4 \times n_{CH_4,in} + 7 \times n_{C_2H_6,in} + \cdots \quad (7)$$

where $n_{H_2,in}$ represents the molar flow rate of H_2 present in the sweet gas; $1 \times n_{CO,in}$ corresponds to the amount of H_2 that can potentially be generated from CO in the sweet gas via the shift reaction (Eq. (5); $4 \times n_{CH_4,in}$ represents the molar flow rate of H_2 obtainable from CH4 present in the sweet gas, with higher hydrocarbons behaving analogously to CH4 in this context. The utilization factor U_f is defined as: $U_f = n_{H_2,consumed}/n_{H_2,equivalent}$, where $n_{H_2,consumed}$ represents the molar flow rate of H_2 used in the electrochemical reaction described in (Eq. (3).

Unreacted fuel (stream 7) and depleted air (stream 13) combust completely in the adiabatic "Afterburner" Rstoic reactor, with heat output (Q5) transferred to the exhaust (stream 14) via "Heater 2". The "Recuperator" block then recovers this heat to preheat the incoming air, while the final exhaust exits as stream 15. The reactions specified in the "Afterburner" block include [33]:

Hydrogen oxidation :

$$H_2 + \frac{1}{2}O_2 \Rightarrow H_2O \quad (8)$$

Carbon monoxide oxidation :

$$CO + \frac{1}{2}O_2 \Rightarrow CO_2 \quad (9)$$

For a better understanding of this process, a schematic diagram illustrating the process flow diagram with heat flow is shown in Fig. 3.

2.2.1. Voltage, fuel flow rate and efficiency calculation The calculation of cell voltage is a key aspect of fuel cell modeling. In this approach, documented in [28,29], a performance curve derived from experimental data under standard reference conditions is used, and the same methodology is applied in the present study. This reference curve is then adjusted with semi-empirical correlations to reflect actual operating conditions, eliminating the need for complex physical or geometric cell parameters. This simplifies calibration and allows easy updates as SOFC materials and designs evolve [34]. The experimental reference curve is taken from the Fuel Cell Handbook [35], and four semi-empirical equations are applied to adjust the reference voltage for deviations from those conditions. The effects of operating pressure, operating temperature, current density, fuel composition, and oxidant composition are represented by the four semi-empirical equations given in Eqs. (10) –(13), respectively.

$$\Delta V_p(mV) = 76 \times loglog\frac{P}{P_{-r}}$$

(10)

where P and P_{ref} represent the operating pressure (bar) and the reference operating pressure respectively (here $P_{ref} = 1$ bar).

$$\Delta V_T(mV) = 0.008 \times (T - T_{ref}) \times I_c \tag{11}$$

where T and T_{ref} are the operating temperature and the reference operating temperature (here $T_{ref} = 1000$° C), and I_c is the current density.

$$\Delta V_{anode}(mV) = 172 \times log\frac{P_{H_2}/P_{H_2O}}{(P_{H_2}/P_{H_2O})_{ref}}$$

(12)

where P_{H_2}/P_{H_2O} represents the ratio of H_2 to steam partial pressures, while $(P_{H_2}/P_{H_2O})_{ref}$ denotes the same ratio under the reference conditions, which in this case is 0.15.

$$\Delta V_{cathode}(mV) = 92 \times log\frac{P_{O_2}}{(P_{O_2})_{ref}}$$

(13)

Here, P_{O_2} represents the average oxygen partial pressure at the cathode under actual operating conditions, while $(P_{O_2})_{ref}$ denotes the corresponding value under reference conditions, which is 0.164 in this case.

The actual cell voltage (V) is the sum of the reference voltage and all adjustments:

$$V = V_{ref} + \Delta V_p + \Delta V_T + \Delta V_{anode} + \Delta V_{cathode}$$

(14)

The equivalent hydrogen flow rate ($n_{H_2,equivalent}$) is derived from the current [33]:

$$n_{H_2,equivalent}\left(\frac{mol}{h}\right) = \frac{n_{H_2,consumed}}{U_f} = \left(\frac{current}{2U_fF}\right) \times 3600$$

$$= \frac{0.018655 \times current}{U_f}$$

(15)

The required sweet gas flow rate is then calculated using the fuel composition [33]:

$$n_{sg}(mol/h) = \frac{n_{H_2,equivalent}}{C_{H_2} + C_{CO} + 4 \times C_{CH_4} + 7 \times C_{C_2H_6} + \cdots}$$

(16)

The power output is determined by multiplying voltage and current. In this model, voltage and power are calculated based on a given current

derived from the current density and cell size. The cell electrical efficiency is given by [33]:

$$\eta_{el,SOFC} = \frac{Power}{n_{sg} \times \underline{LHV}_{sg}} = \frac{current \times V}{n_{sg} \times \underline{LHV}_{sg}}$$

(17)

The SOFC converts only a portion of the fuel' s chemical energy into electricity, while the remaining energy is released as heat due to system losses. Part of this heat is utilized to preheat the incoming fuel and air streams, and a considerable portion supports the endothermic reforming reaction. To maintain a stable cell temperature, additional airflow is supplied to cool the stack. In Aspen Plus, the net heat duty (Q4) of the "ANODE" block is automatically calculated to account for these heat effects [33]:

$$Q_4 = Q_e + Q_s + Q_r + Q_g (18)$$

where *Qe* represents the heat from the electrochemical reaction, *Qs* is the heat of the water–gas shift reaction, *Qr* corresponds to the reforming reaction heat, and *Qg* denotes the heat transferred to the fuel and air streams. Considering a specified heat loss (*Ql*), the required airflow to maintain the stack temperature can be determined by introducing a design-spec in Aspen Plus, which satisfies the following equation [33]:

$$Q_4 - Q_l - W_{elec} = 0 \quad (19)$$

2.2.2. Validation

The proposed model was validated by performing a simulation of a 100 kW atmospheric SOFC stack consisting of 1152 cells, following the methodology reported in Ref. [30–32]. Key calculation results and comparisons with published data are presented in Table 2, demonstrating that the SOFC model, built using Aspen Plus operation modules, can effectively predict stack performance. Reasonable assumptions were made to align the simulation with reference studies. The inlet fuel composition (mole basis) was set as CH4 81.3%, C2H6 2.9%, C3H8 0.4%, C4H10 0.2%, N2 14.3%, and CO 0.9%. Inlet air and fuel temperatures were set at 630 ◦ C and 200 ◦ C, respectively. The total active area, corresponding to the 1152 cells, was set at 96.1 m2 [33]. Under these conditions, the SOFC produces 121.28 kWe of DC power at an efficiency of 53.25%. As shown in Table 2, the observed deviations are below 1.29% and average 0.72%, clearly stating the validity of the model.

Table 2 SOFC model results compared to Ref [33].

Parameters	Zhang et al[33]	Model simulationdata	Deviation(%)
Voltage, [mV]	700	709.01	1.29
Current density, [mA.cm− 2]	178	178	–
Pre-reformer outlettemperature, [◦ C]	536	535.65	0.07
Pre-reformer CH4conversion, [%]	25.9%	26.05%	0.58
Cathode inlet temperature,[◦ C]	821.32	823.967	0.32
Combustion productstemperature, [◦ C]	1012.35	1012.73	0.04
Stack exhaust temperature,[◦ C]	834	833.96	0.005
Anode outlet composition,	50.9% H2O	50.90% H2O	–
[stream 5]	24.9% CO2	24.97% CO2	

Parameters	Zhang et al[33]	Model simulationdata	Deviation(%)
	11.6% H2	11.61% H2	
	7.4% CO	7.38% CO	
	5.1% N2	5.14% N2	
Stack exhaust composition	77.3% N2	77.26% N2	–
[stream 15]	15.9% O2	15.84% O2	
	4.5% H2O	4.55% H2O	
	2.3% CO2	2.35% CO2	
Power output, [kW]	120	121.28	1.07
Gross AC efficiency [LHV]	52%	53.25%	2.40

2.3. Micro gas turbine

The AE-T100 micro gas turbine, whose schematic is shown in Fig. 4, operates on a recuperated Brayton cycle in which air is first compressed (pressure ratio 3–5), preheated using turbine exhaust heat in a recuperator, and then heated up to 950 ◦ C, the maximum turbine inlet temperature (TIT) without blade cooling. The high-temperature gases expand through the turbine, providing the power needed to run both the compressor and the generator. At the same time, residual exhaust heat is recovered for combined heat and power (CHP) applications, such as heating water from 50 ◦ C to 70 ◦ C. Exhaust gas recirculation can raise the CO2 concentration from 1.7% to 4.3% by recycling cooled and filtered flue gas; the EGR pathway is illustrated in Fig. 4 using orange lines. The numerical simulation of the mGT with EGR follows the approach developed by De Paepe et al. [21], where the baseline model (without EGR) was experimentally validated, and the same validated model is applied in the present study.

In this study, a hybrid mGT + SOFC system is employed, in which a heat exchanger replaces the conventional combustion chamber. The SOFC provides the necessary heat, eliminating the need for a combustion chamber. Further details on this configuration are presented in Section 3.3.

2.4. Carbon capture

The carbon capture efficiency achieved in the present system is approximately 90%, which is consistent with conventional amine-based post-combustion capture technologies. Typically, absorption-based systems using solvents such as monoethanolamine (MEA) achieve CO2 removal efficiencies in the range of 85–95% under standard operating conditions [36]. The amine-based absorption method was selected due to its high technological maturity, reliability, and suitability for postcombustion CO2 capture under moderate temperature and pressure conditions. Compared to other mainstream technologies such as membrane separation, adsorption, and cryogenic processes, absorption systems offer higher capture efficiency, stable operation, and lower sensitivity to variations in CO2 concentration [37]. In addition, this technology has been extensively validated at industrial scale, making it a practical and realistic choice for integration with the proposed SOFCbased system. The conventional absorption-based carbon capture system consists of two main units: an absorber and a stripper, as presented in Fig. 5. The process begins with cooled flue gases (1) entering the bottom of the absorber, while a lean amine-based solvent is fed at the top (2). Inside the absorber, CO2 is chemically absorbed by the solvent at 40 ◦ C and atmospheric pressure, producing a CO2-rich solvent stream at the bottom. The treated gas, with 90% CO2 removal, exits from the top. The rich solvent is then pressurized (3) and preheated in a heat exchanger (4) by the regenerated solvent returning from the stripper. It then enters the stripper (5), where heat supplied by the reboiler (6) breaks the CO2-solvent bonds at 100–150 ◦ C and 1.2–5 bar, depending on the solvent. The released CO2 exits the stripper, is condensed to remove water (7), and reaches a purity of 98%. The regenerated solvent is recirculated (8) through the heat exchanger (4) and a cooler (9) before returning to the absorber. Additionally, a makeup stream containing water and amine is supplied to compensate for solvent losses occurring during the process [27].

The carbon capture plant was modeled using data from the PACT1 pilot facilities of the UKCCSRC2 [38]. The thermodynamic modeling used the ENRTL model for liquid-phase electrolytes and the PC-SAFT equation of state

for the vapor phase. The thermodynamic parameters applied in these models were obtained from [24]. The absorber and stripper were simulated using RadFrac' s rate-based approach [39],

1 Pilotscale Advanced Capture Technology.

2 UK Carbon Capture and Storage Research Center.

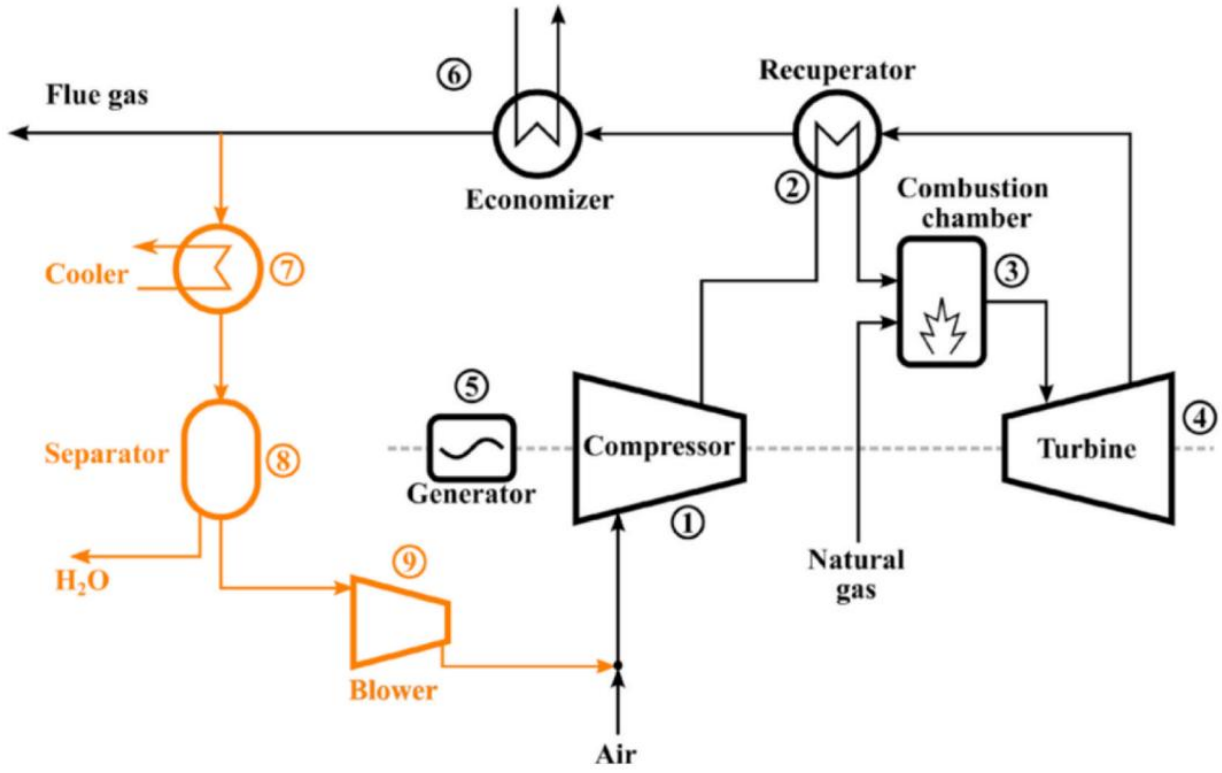

Fig. 4. Schematic of the AE-T100 mGT integrated with exhaust gas recirculation (orange lines) in Ref [21].

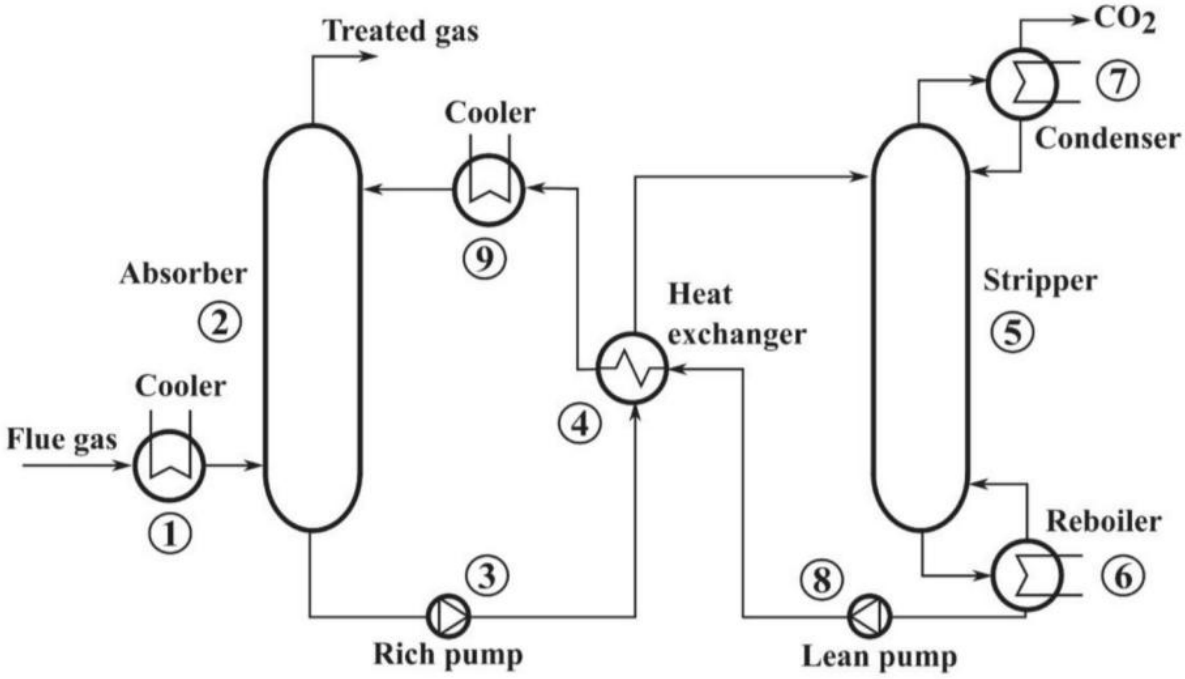

Fig. 5. Process flow diagram of a conventional absorption-based CC plant [27].

incorporating IMTP3 packing material [40] with mass transfer calculated via the Hanley IMTP3 model [41] and heat transfer using Chilton-Colburn correlations. Both columns were divided into 30 stages [27].

The validation of the present model has been comprehensively addressed in Ref. [27]. Accordingly, the validated model from that work is adopted here, and there is no need to repeat the validation procedure, as it has already been confirmed.

3. Results and discussion

Following the detailed system characterization and unit validation procedures, this section systematically examines the simulation outcomes, tracing the complete process chain from upstream flare gas sweetening to downstream CO2 capture operations.

3.1. Step 1. Gas sweetening unit

Following successful unit validation using reference gas data and literature-reported parameters, the flare gas specifications for this study, as presented in Table 3, were introduced into the system. Among the various flare gas compositions reported in Ref. [8] the selected sample corresponds to a gas refinery stream characterized by a relatively high CO2 content (29.54 mol%) and a significant H2S fraction (5.38 mol%). This composition was intentionally selected to represent a challenging and realistic industrial scenario. The elevated H2S concentration justifies the integration of a gas sweetening unit prior to energy conversion, while the high CO2 fraction makes the subsequent carbon capture stage technically meaningful. The flare gas composition listed in Table 3 was defined as the feed stream to the gas sweetening unit under steady-state

3 Intalox Metal Tower Packings.

Table 3 Specifications of the flare gas examined in this study [8].

Parameter			Composition [Molar %]							
Temperature [◦ C]	Pressure[bar]	Flow rate [MMSCFD]	N2	H2S	CO2	CH4	C2H6	C3H8	C4+	H2O
19.00	1.00	13.61	1.80	5.38	29.54	62.53	0.36	0.06	0.15	0.00

conditions. The ENRTL thermodynamic property method was employed to model the absorption process, as it is well-suited for electrolyte systems involving acid gases such as CO2 and H2S and aqueous amine solutions. The sweetening process was carried out using the same operating conditions, solvent properties, and simulation methodology as the validated model described previously. Only the inlet flare gas composition and flow conditions were modified according to the selected case presented in Table 3.

In this section, the system performance is analyzed through two operational variables: absorber packing height and lean solvent circulation rate. The H2S concentration in the sweet gas depends heavily on the lean solvent recirculation rate across six absorber packing heights (see Fig. 6). Each packing height (h = 20–30 m) produces a distinct curve showing that higher packing heights consistently achieve lower H2S concentrations at equivalent solvent flow rates. The inverse relationship demonstrates that increased solvent circulation improves H2S removal efficiency, while greater packing heights enhance the surface area of the packing, with the 30 m column showing the best performance across all flow rates. The results quantitatively demonstrate how optimizing both solvent flow and packing height can significantly improve sweetening process efficiency. The industrial standard requires less than four ppm H2S in the sweet gas [8]. Previous studies have shown that H2S in the low ppm range causes only short-term and reversible voltage drops in the fuel cell [36–38]. Therefore, further removal is unnecessary, and a concentration of less than four ppm is suitable for the present hybrid system. Consequently, for each packing height, the minimum allowable solvent flow rate meeting this specification was determined and presented in Table 4. As shown, the 30 m packing height meets the target with a solvent flow of 0.29 kg/s, corresponding to the lowest reboiler duty, and was therefore selected as the optimal operating condition. The simulation stream results of this case are presented in Fig. 7.

3.2. Step 2. Sensitivity analysis for SOFC

In this step, the sweet gas from the previous unit is fed to the SOFC.

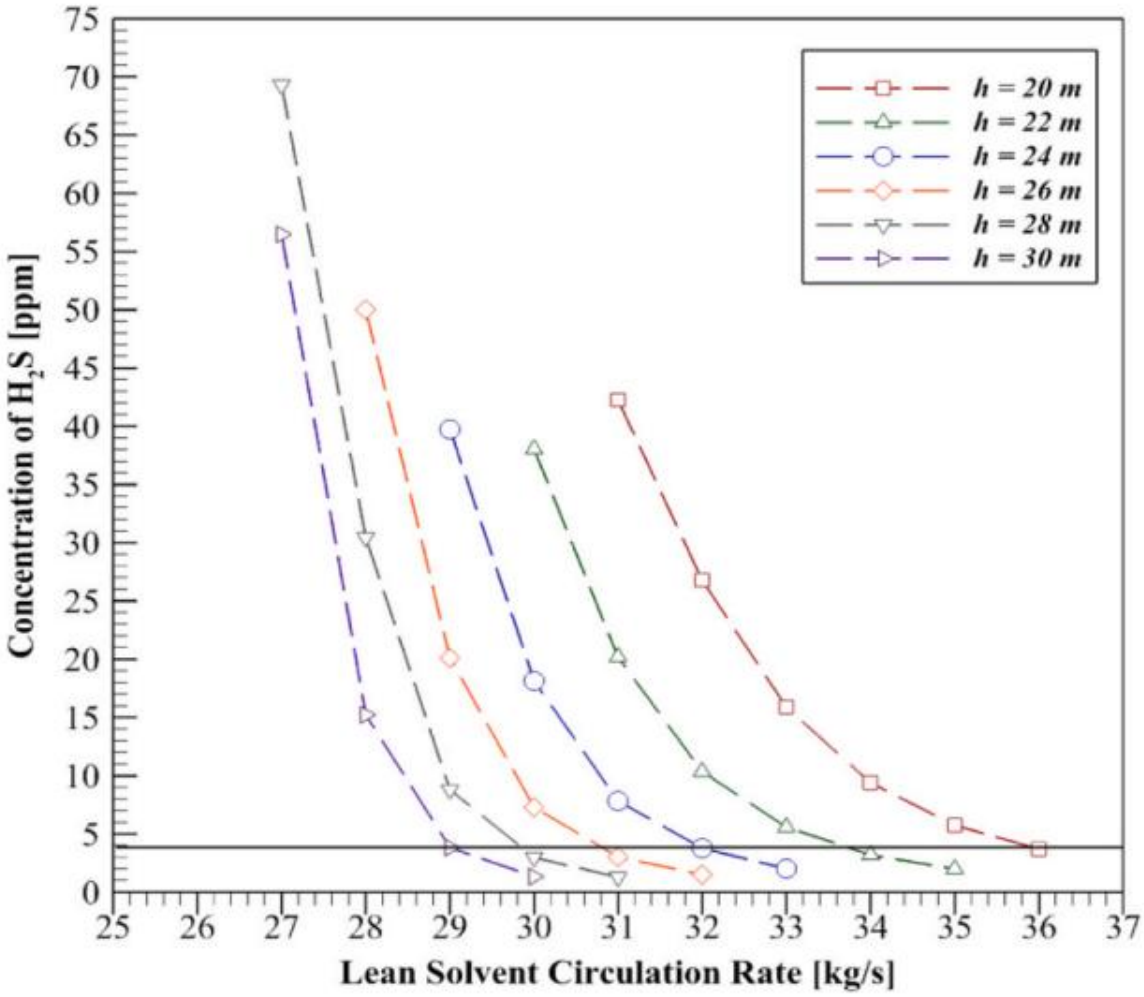

Fig. 6. Variation of H2S concentration in sweet gas [ppm] with lean solvent circulation rate [kg/s] for different absorber packing heights (h = 20–30 m).

Table 4 Acceptable lean solvent flow rates and corresponding parameters for each packing height (optimal values in italics).

Height[m]	Lean SolventFlow rate[kg/s]	H2SConcentration[ppm]	CO2Concentration[mol%]	ReboilerDuty[MW]
20	36	3.683	0.042	17.46
22	34	3.212	0.034	16.93
24	32	3.765	0.037	16.32
26	31	3.034	0.028	15.94
28	30	2.980	0.025	15.50
30	29	3.823	0.029	15.02

The input flow rate is determined based on the SOFC' s specifications, ensuring only the required portion is supplied. Before integration with the micro gas turbine, it is necessary to examine the effect of key operating parameters; therefore, a sensitivity analysis is conducted for several critical variables.

Fig. 8(a) illustrates the impact of current density variation on cell voltage, power, efficiency, inlet air flow, and fuel flow at a constant fuel utilization factor (*Uf* = 0.85). It should be noted that the selected current density range (160–250 mA/cm2) is consistent with the operating conditions of the validated reference SOFC stack model described in Section 2.2.2 and Ref. [33]. Since the present model is based on a validated 100 kW atmospheric SOFC stack, the current density was varied within its realistic and experimentally verified operating range to ensure reliable and physically meaningful performance predictions. As the current density rises, the cell voltage declines linearly due to heightened ohmic and activation losses. Consequently, the efficiency (which is directly dependent on the product of *V* and *Uf*) exhibits a corresponding reduction. Despite the efficiency drop, the total power output increases significantly with current density, driven by the higher electrochemical reaction rates. This necessitates a proportional rise in inlet fuel flow to meet the increased demand for reactants. Simultaneously, the air flow must increase to supply sufficient oxygen ions for the electrochemical reactions and to dissipate the additional heat generated by irreversible losses. The latter effect is primarily attributed to increased irreversible losses at higher current densities, which convert a larger fraction of chemical energy into heat, thereby increasing the cooling requirement of the inlet air stream. Lower current densities promote efficiency but reduce the output per unit cell area. Therefore, to achieve the same total power output at higher current densities, a larger active cell area is required, which incurs higher capital costs. This trade-off highlights the importance of selecting an optimum current density that balances efficiency, system size, and economic considerations.

The fuel utilization factor strongly influences the operating performance of fuel cells. This parameter also plays a crucial role in determining the concentration of unburned fuel in exhaust gases, which is particularly important for CO2 capture processes. To identify the optimum fuel utilization factor, a parametric study was conducted, and key performance indicators including voltage, power output, efficiency, and CO2 concentration were evaluated. The optimum value was selected based on achieving a balance between maintaining high electrochemical performance and ensuring sufficient CO2 concentration for effective carbon capture, while avoiding excessive polarization losses and fuel starvation. Fig. 8(b) depicts the effect of fuel utilization factor on the same important operational parameters at a constant current density of 178 mA/cm2 . This graph shows that an increase in *Uf* from 0.65 to 0.95

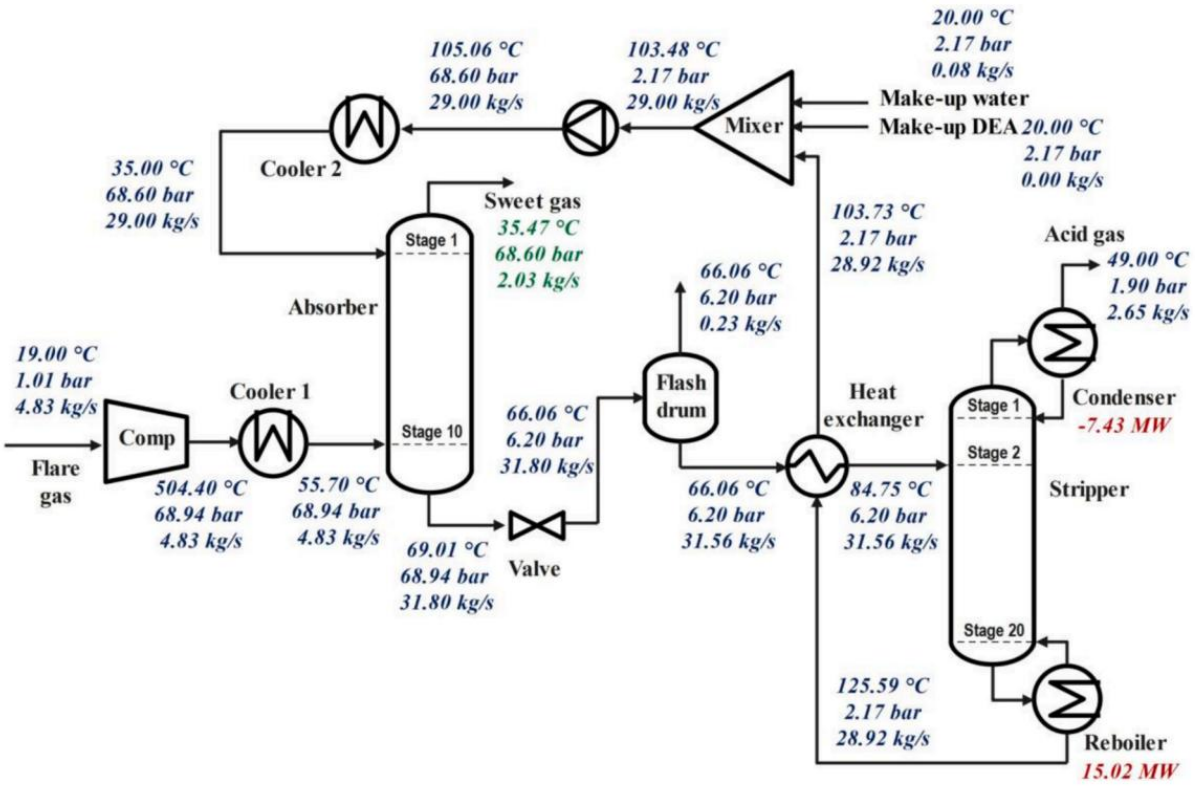

Fig. 7. Temperatures, pressures and mass flows at all streams of the gas sweetening unit for optimum case.

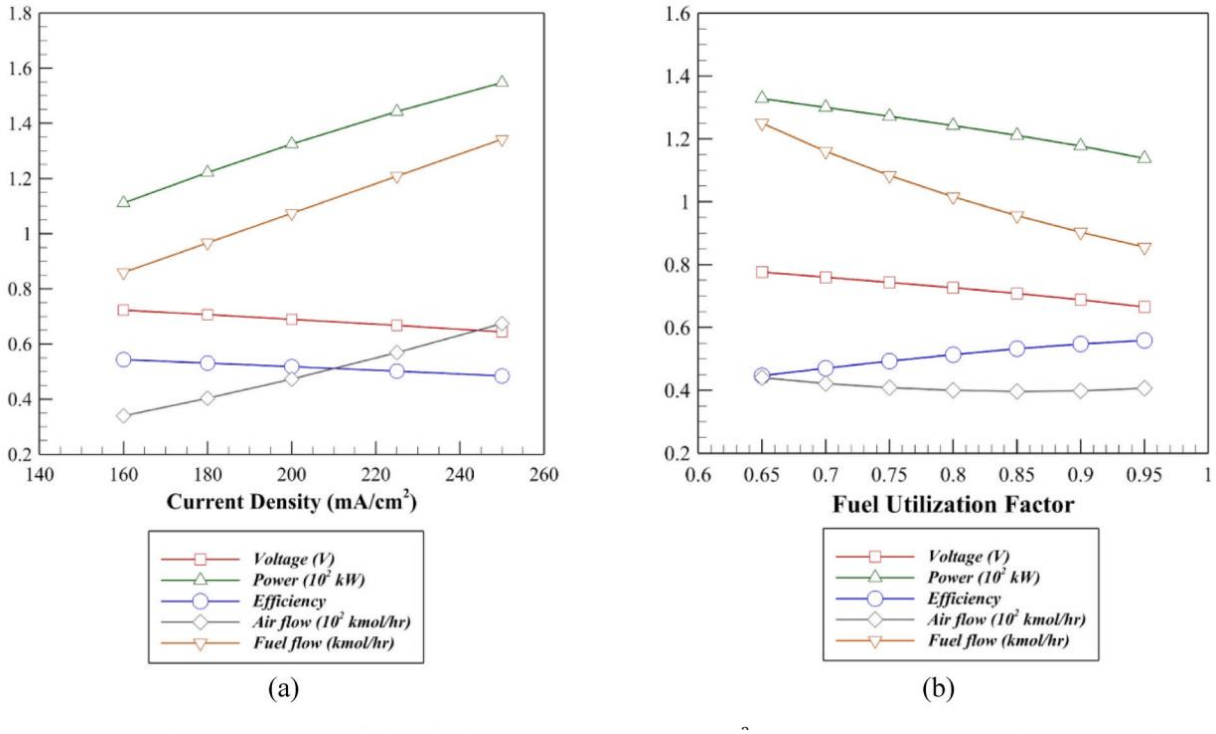

Fig. 8. Effect of (a) current density (Uf = 0.85) and (b) fuel utilization factor (Ic = 178 mA/cm2) variation on SOFC operational parameters (voltage, power DC, efficiency, inlet air flow, and fuel flow).

causes a significant voltage drop. In practice, increasing fuel utilization in SOFC leads to trade-off phenomena that dictate total performance. The system extracts more energy out of each molecule as more fuel is burned, leading to greater efficiency. This comes at the cost of reduced fuel concentration at the anode, leading to a shortage that diminishes the electrochemical reactions. This starvation of fuel lowers the voltage

gradually, which naturally decreases the power output since the current remains constant. The air supply is more complex in its action, trending downwards before trending upwards as the system tries to compensate for the changing conditions. There is an optimal middle point where the benefit of better fuel efficiency balances the drawback of voltage loss, typically at moderate usage levels. On the other side of this point is the

danger of fuel depletion, damage to the cell with diminishing returns, and below it is wasted potential energy from unburnt fuel. These inherent trade-offs underscore the importance of precisely controlling fuel consumption to achieve a balance between performance, efficiency, and longevity in SOFC operation.

As shown in Fig. 9(a), the anode exhaust composition changes significantly with increasing fuel utilization factor. As U_f rises from 0.65 to 0.95, the concentrations of unburned fuel components (CO and H_2) steadily decrease while reaction products (CO $_2$ and H_2 O) progressively increase, with N_2 concentration remaining essentially constant. This trend confirms that higher U_f leads to more complete fuel oxidation, resulting in greater CO $_2$ production, which is beneficial for carbon capture. The analysis indicates that while higher fuel utilization increases CO $_2$ production, it compromises cell voltage and power due to polarization losses. An operating point of $U_f = 0.85$ offers the most balanced trade-off, providing sufficient CO $_2$ concentration for capture and maintaining superior performance compared to higher utilizations. At this level, fuel starvation is avoided, fuel conversion remains efficient, and N_2 primarily acts as an inert diluent in the exhaust.

The steam-to-carbon (S/C) ratio at the pre-reformer inlet must be carefully controlled to prevent carbon formation while optimizing system performance. Defined as the molar ratio of H2O molecules to carbon atoms in the fuel [35], the S/C ratio is adjusted through depleted fuel recirculation. As shown in Fig. 9(b), increasing the

S/C ratio from 1.5 to 6.5 raises the pre-reformer inlet temperature due to the increased recirculation of high-temperature depleted fuel, simultaneously enhancing methane conversion via steam reforming reactions. This results in higher fuel stream temperatures exiting the adiabatic prereformer, beneficially reducing thermal gradients in the SOFC stack. However, these advantages come with significant trade-offs: higher S/Cratios lower single-pass fuel utilization (although 85% overall utilization is preserved) by increasing total fuel flow, and require larger prereformer and stack sizes, thereby increasing capital costs [33]. Consequently, the optimum S/C ratio is a compromise between minimizing carbon deposition, managing thermal stresses, and minimizing equipment expenses. A sensitivity analysis was performed for S/C ratios between 1.5 and 6.5 to evaluate their effects on reforming performance and thermal conditions. The optimum value was selected as the minimum S/C ratio that ensures stable reforming, avoids carbon formation,

and prevents unnecessary increases in recirculation and system size. Based on these criteria, an S/C ratio of 2.5 was selected for subsequent simulations. It is typically located at the lowest ratio that satisfies both material and thermal uniformity criteria.

The stream results of the selected case for further study are presented in Fig. 10. These operating conditions were selected based on the above sensitivity analyses and trade-off evaluation. The red dashed lines illustrate heat flow among different components, and the operating conditions considered for this unit in subsequent simulation steps are $U_f = 0.85$, $I_c = 178$ mA/cm2, and S/C = 2.5.

3.3. Step 3. Performance of the mGT combined with SOFC In order to increase energy efficiency and utilize the waste heat output from the SOFC, the integration of this unit with a 100 kW_e micro gas turbine (AE-T100) is investigated in this section. In addition, as shown in Fig. 13, the use of the EGR valve (red lines) in this hybrid system results in an increase in the output carbon dioxide concentration and more efficient carbon capture. In the proposed configuration, the SOFC is positioned downstream of the turbine, resulting in improved operational stability and easier control, particularly by reducing surgerelated risks.

As illustrated in Fig. 11, the hot gases exiting the SOFC pass through the "Recuperator" and subsequently enter the "Heat Exchanger" of the mGT (orange lines), where they supply the required turbine inlet temperature for power generation in this unit. The residual heat in the "Preheater" is given to the compressor outlet air. Finally, the residual heat in this gas is used to preheat the sweet gas entering the SOFC. In addition, the red lines in this figure represent the EGR valve, through which a fraction of the gases originally directed toward the carbon capture are recirculated into the cycle according to the specified EGR ratio. In the EGR, after passing through "Cooler 2" , it is cooled to a specific temperature (in this study, three different temperatures of 15°C, 25°C, and 35°C were investigated) and then discharged into the excess "Separator" . The existing "Blower" compensates for the pressure drop in the gas path after the SOFC exits, and this loop is closed by mixing the gases with the air entering the compressor.

The following assumptions were applied to both the mGT and the SOFC. Ambient conditions were fixed at 1.013 bar and 15°C. The

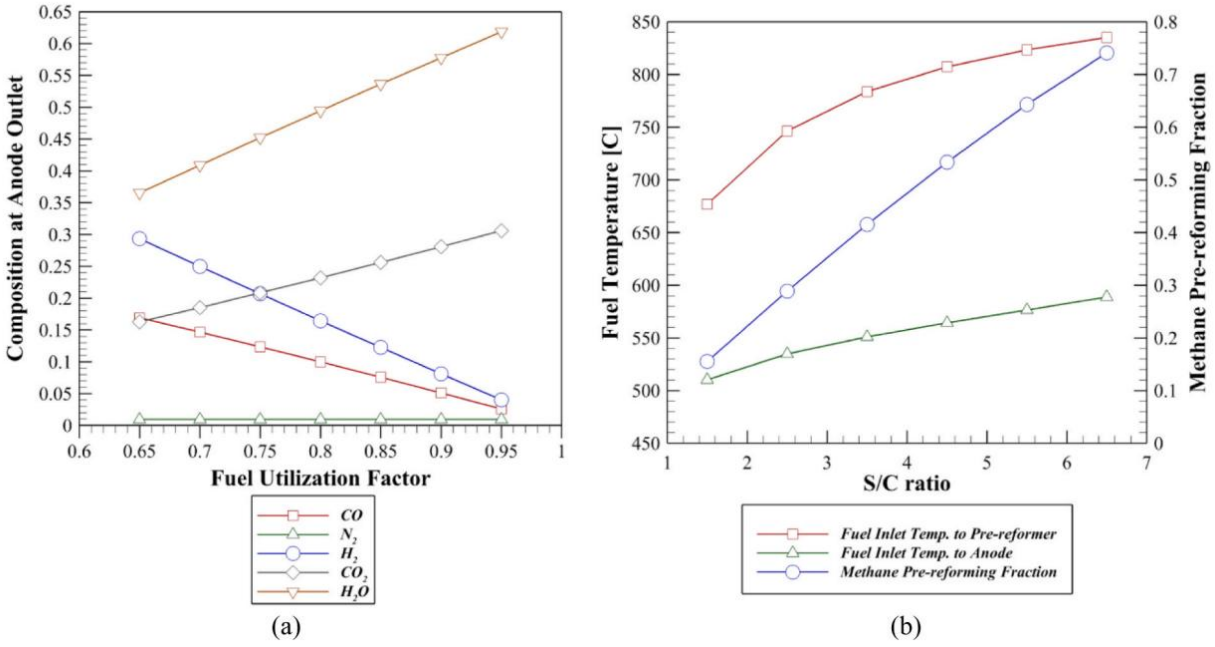

Fig. 9. (a) Effect of fuel utilization factor variation on the composition at the anode outlet under constant current density ($I_c = 178$ mA/cm^2), (b) Effect of steam-to-carbon ratio on the pre-reformer inlet temperature, anode feed temperature, and methane conversion rate in pre-reforming.

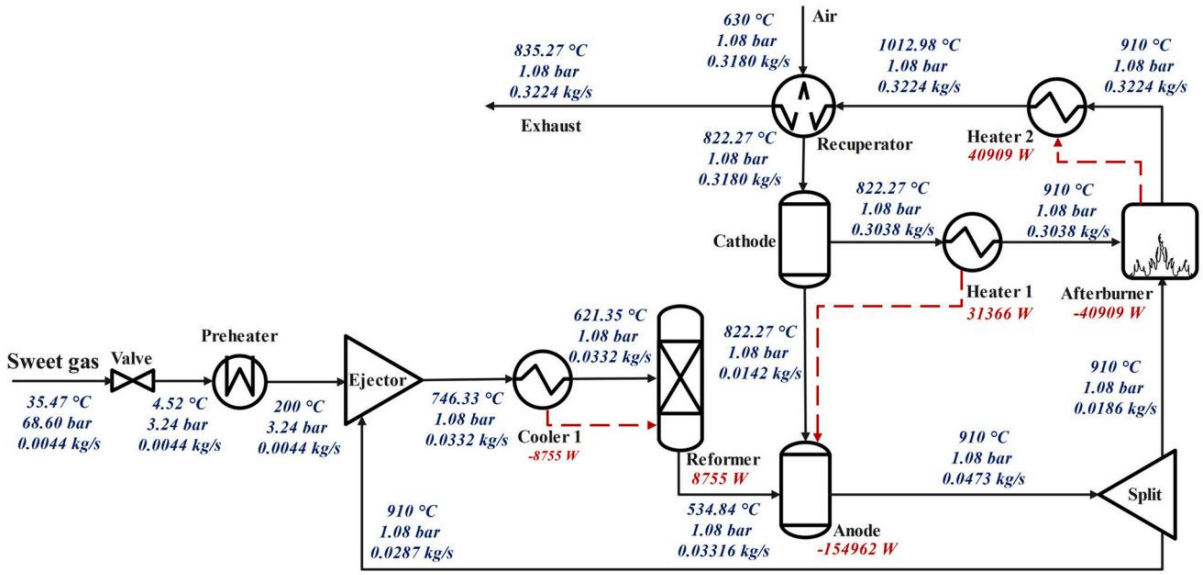

Fig. 10. The SOFC simulation results (Uf = 0.85, Ic = 178 mA/cm2 , S/C = 2.5).

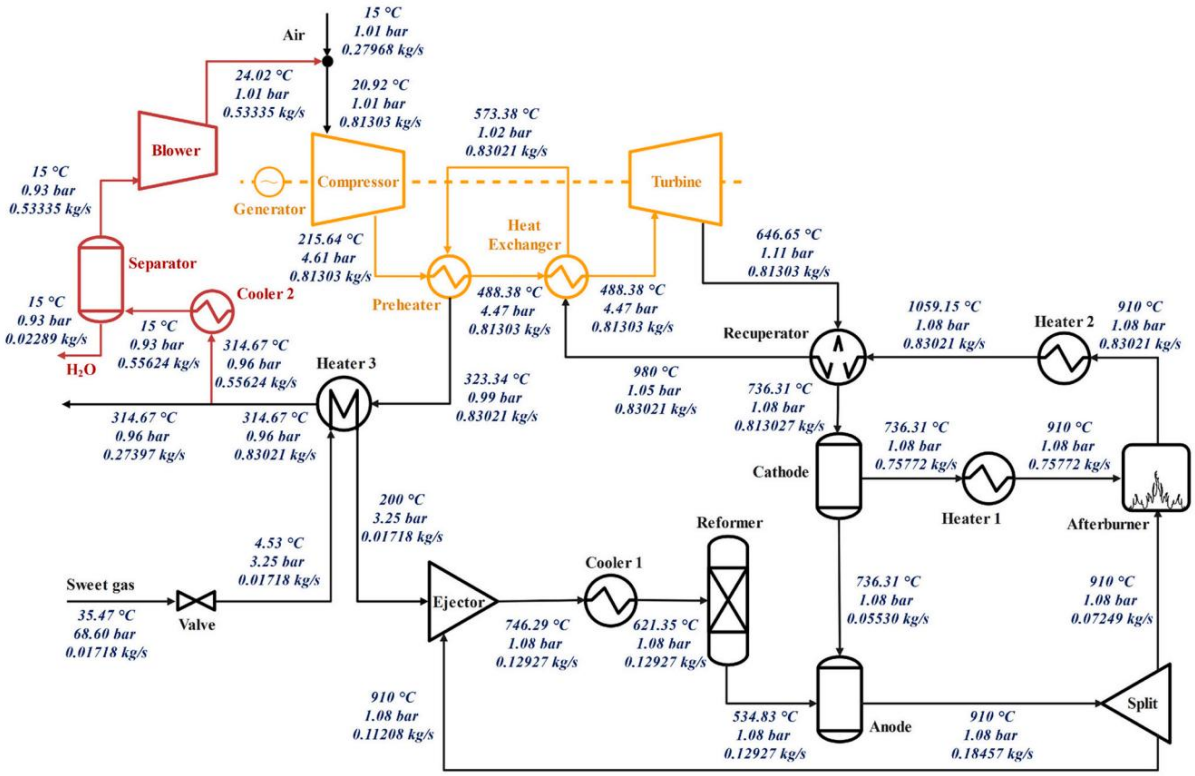

Fig. 11. Process flow diagram and streams results of mGT + SOFC + EGR system with EGR ratio = 0.67 and EGR cooling temperature = 15 ◦ C.

compressor was modeled based on real compressor performance using quasi-dimensionless and corrected parameters, including isentropic efficiency, pressure ratio, corrected mass flow rate, and corrected rotational speed (similar compressor maps are available in [42]). The compressor' s mechanical efficiency is assumed to be 99%. The turbine is considered choked, operating with an isentropic efficiency of 85% and a

mechanical efficiency of 99%. For the high-speed generator and its associated power electronics, a total conversion efficiency of 94% is assumed to match the grid voltage and frequency. For SOFC, the simulation assumptions are similar to those mentioned in Ref. [33]. The only important difference in the design of this hybrid system compared to the alone SOFC is that here it is not possible to control the air entering the

SOFC (in the cathode side), since the amount of air entering the system is determined by the mGT, so in order to establish an energy balance in this unit according to Eq (19), the amount of active area in this unit is adjusted. The boundary conditions used in the simulation of the hybrid system are fully listed in Table 5. To better understand this concept, a schematic diagram of the hybrid system' s convergence, which includes several calculation loops, is shown in Fig. 12.

As shown in Fig. 12, the model includes two types of loops: a design specification loop (shown with a dashed line) and a physical loop (shown with a solid line). The design specification loop adjusts an input parameter to achieve a target variable value, while the physical loop represents actual process recycles. Design loop "A"adjusts the inlet air mass flow rate to ensure that choking conditions are achieved at the turbine inlet. The physical loop "B" takes into account the heat exchange in the "Heat Exchanger" , which will influence the temperature in the turbine inlet. The physical loop "C" takes into account the heat exchange in the "Preheater" , which affects the temperature entering the "Heat Exchanger" . The design loop "D" changes the rotational speed of the shaft to have the requested power output of the mGT (100 kWe). The design loop "E" changes the output temperature of "Reformer" to have the same heat duty in both "Cooler 1" and "Reformer" . The design loop "F" changes the split fraction of "Split" to have the desired amount for S/C ratio in SOFC. The physical loop "G" means that

part of the anode exit flow is recirculated in the "Ejector" inlet. Finally, in the physical loop "H", a fraction of the exhaust gas is routed back to the "Compressor" inlet.

3.3.1. Sensitivity analysis

Now, the effects of variations in the EGR ratio and its cooling temperature on the design parameters of the hybrid system are examined. The relative amount of recirculating exhaust gas is expressed as:

Table 5 Operating conditions used in the Aspen Plus simulations for hybrid mGT + SOFC + EGR.

mGT Operational Parameter[40,41]	Value	SOFC OperationalParameter [33]	Value
Inlet air temperature of thecompressor	15 ◦ C	Cell operating pressure	1.08 bar
Inlet air pressure of thecompressor	1.013bar	Ejector pressure ratio	3
Compressor mechanicalefficiency	99%	Active area	Variableb
Corrected air flow rate ofthe compressor	Variablea	Cell operatingtemperature	910 ◦ C
Isentropic efficiency of thecompressor	Variablea	Inlet fuel temperature	200 ◦ C
Pressure ratio	Variablea	Overall fuel utilizationfactor	85%
Turbine isentropicefficiency	85%	S/C ratio	2.5
Turbine mechanicalefficiency	99%	Current density	178 mA/cmb
Turbine Inlet Temperature(TIT)	930	Pressure drops insidethe SOFC	0
Choking constant of theturbine	6.5	"Afterburner" efficiency	100%
Combined generator andpower electronicsefficiency	94%	"Recuperator" hotoutlet temperature	980 ◦ C
Produced electrical power	100 kWe	SOFC thermal losses	2%
Cold side and hot sidepressure loss in heatexchangers	3%	DC to AC inverterefficiency	92%
"Heat Exchanger" pinchpoint temperature	50 ◦ C	EGR CoolingTemperature	15 ◦ C, 25 ◦ C,35 ◦ C

Now, the effects of variations in the EGR ratio and its cooling temperature on the design parameters of the hybrid system are examined. The relative amount of recirculating exhaust gas is expressed as:

a Generic compressor maps were employed in the simulations.

$$EGRratio = \frac{\dot{V}_{EGRstream}}{\dot{V}_{exhaustgas}} \quad (20)$$

where, $\dot{V}$ *EGRstream* and $\dot{V}$ *exhaustgas* are flow rate of EGR stream and exhaust gas, respectively.

Fig. 13(a) presents the variation of the SOFC unit active area as a function of the EGR ratio at three cooling temperatures, namely 15 ◦ C, 25 ◦ C, and 35 ◦ C. With increasing EGR ratio at 15 ◦ C, the active area of the SOFC remains nearly constant up to an EGR ratio of 0.15, after which it gradually decreases. At the highest EGR ratio (0.67), the active area drops significantly, by approximately 10% compared to the case without EGR. At 25 ◦ C, the active area initially increases with EGR ratio and reaches a peak around an EGR ratio of 0.4, followed by a downward trend. At an EGR ratio of 0.65, it decreases to about 2.8% below the initial value. At 35 ◦ C, the active area consistently increases with higher EGR ratios, reaching approximately 8% above the baseline value at an EGR ratio of 0.44.

The effects of the EGR ratio and temperature on the mGT + SOFC + EGR electrical power and blower power consumption are analyzed. Fig. 13(b) shows the variations of these two quantities at three cooling temperatures. It should be noted that the total electrical power refers to the combined output power from the SOFC and the 100 kWe mGT. At 15 ◦ C, as the EGR ratio increases, the electrical power initially remains almost constant and then decreases; at the highest EGR ratio (0.67), a 14% reduction occurs compared to the case without EGR, while the blower power rises linearly to about 4.9 kWe. At 25 ◦ C, the electrical power slightly increases (<0.5%) up to an

EGR of 0.25–0.30, then declines; at 0.65, it is ~8% lower than the initial value, whereas the blower power rises to about 5.2 kWe. At 35 ◦ C, the electrical power gradually increases, reaching ~ 4% above baseline at an EGR ratio of 0.44, while the blower power increases up to 3.8 kWe. For all temperatures, blower power growth results from the higher flow rate of recirculated exhaust gas, which increases pressure-drop compensation demand.

Fig. 14(a) shows that increasing the EGR ratio causes a clear decline in the mGT + SOFC + EGR electrical efficiency at all cooling temperatures. For 15 ◦ C, efficiency gradually decreases from 64.07% (without EGR) to 60.36% at an EGR ratio of 0.67, showing an overall reduction of about 5.9%. At 25 ◦ C, the efficiency drops more sharply, falling from 64.07% to 59.82% at an EGR ratio of 0.65, corresponding to a decrease of approximately 6.6%. Meanwhile, at 35 ◦ C, the efficiency shows a less pronounced decline, decreasing from 64.07% at zero EGR to 61.54% at an EGR ratio of 0.44, corresponding to a reduction of approximately 3.9%. The analysis of the results reveals that the reduction in SOFC electrical efficiency at 15 ◦ C and 25 ◦ C with increasing EGR ratio is primarily attributed to the decrease in the SOFC power output. At 35 ◦ C, although the SOFC power output increases with a higher EGR ratio, the enlargement of the active area leads to an increased fuel flow demand (sweet gas flow rate) for the hybrid system, which in turn causes the overall electrical efficiency to decline under this condition as well.

Fig. 14(b) illustrates the mass flow rates of three streams, namely the turbine exhaust, the flow directed to the carbon capture, and the recirculated stream. Solid lines represent the case at 15 ◦ C, while dashed lines correspond to 35 ◦ C. As expected, with increasing EGR ratio, the flow rate to the CC decreases, while the recirculated stream increases. The turbine exhaust flow is nearly constant but shows a slight increase with higher EGR ratios due to the elevated choking flow rate in the turbine, while the inlet air flow is self-adjusted to maintain the net power output of the micro gas turbine equal to 100 kWe. An important observation is that the curves at 35 ◦ C are consistently higher than those at 15 ◦ C for all streams. This is because, at higher temperatures, water removal from the exhaust gas in the EGR separator is incomplete, leading to a higher overall flow rate.

Fig. 15(a) illustrates how the exhaust gas temperature delivered to the carbon capture responds to variations in the EGR ratio for three EGR cooling temperatures. For 15 ◦ C, the exhaust gas temperature climbs

b Calculated based on energy balance according to Eq. (19).

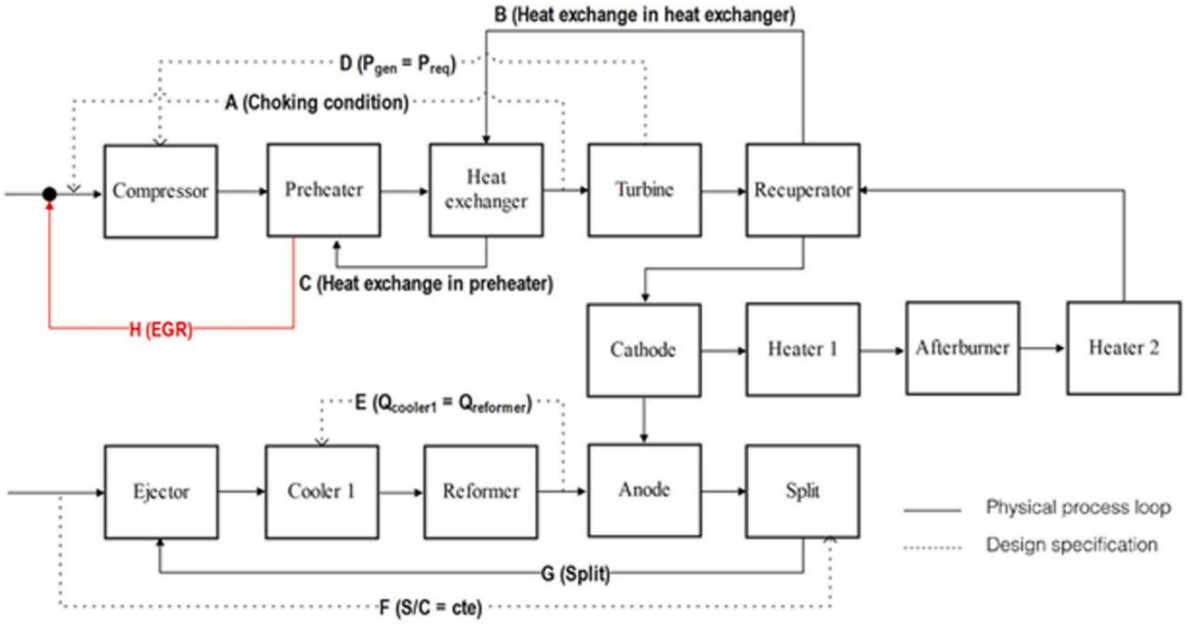

Fig. 12. Flowsheet of the numerical model adopted for mGT + SOFC + EGR.

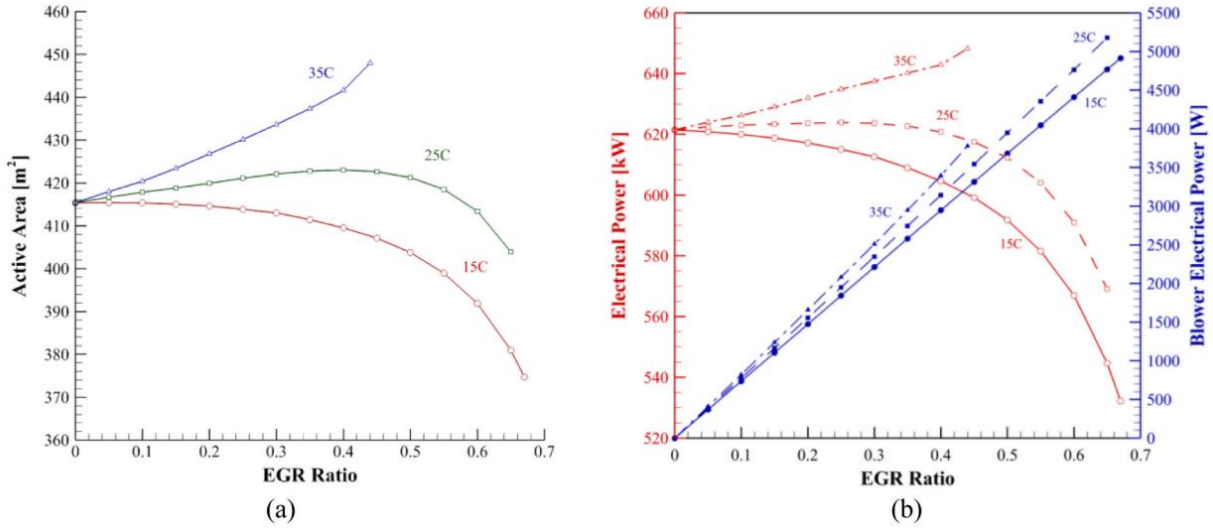

Fig. 13. Variation of (a) SOFC active area and (b) mGT + SOFC + EGR electrical power and blower electrical power as a function of the EGR ratio at three different EGR cooling temperatures.

gently from the baseline value of 313.39 ◦ C, peaks at 317.31 ◦ C when the EGR ratio reaches 0.45, and then falls slightly, remaining roughly 0.4% higher than the initial level at the maximum ratio of 0.67. When the EGR temperature is 25 ◦ C, the rise is more pronounced and essentially monotonic, ending at 333.71 ◦ C for an EGR ratio of 0.65, which represents a 6.5% increase over the condition without EGR. The 35 ◦ C case exhibits the steepest ascent: the exhaust gas temperature increases continuously to 344.35 ◦ C once the EGR ratio reaches 0.44, corresponding to an elevation of almost 9.9% relative to the baseline.

The molar composition of the gases sent to the carbon capture at different EGR ratios is presented in Fig. 15(b). The CO2 fraction increases with higher EGR ratios, rising from 3.94 vol% to 10.78 vol% at an EGR ratio of 0.67. Conversely, the O2 concentration decreases from 12.31 vol% to 0.03 vol% at the same EGR ratio of 0.67. It can also be observed that the EGR temperature and its increase up to 35 ◦ C have only a minor effect on the CO2 and O2 concentrations in the gases entering the carbon capture. However, the water content in these gases increases with higher EGR cooling temperature, since elevated temperature reduces the degree of water condensation, thereby leaving more vapor in the stream.

3.3.2. Technical analysis In the previous section, the results indicated that at a 15 ◦ C EGR cooling temperature, the EGR ratio can be increased up to 0.67 without causing any issues in the combustion process in the afterburner. In this state, the molar fraction of oxygen in the inlet air of "Afterburner" is around 1.2%, and the combustion reactions proceed to completion with no fuel residue in the exhaust. This cooling temperature can be achieved

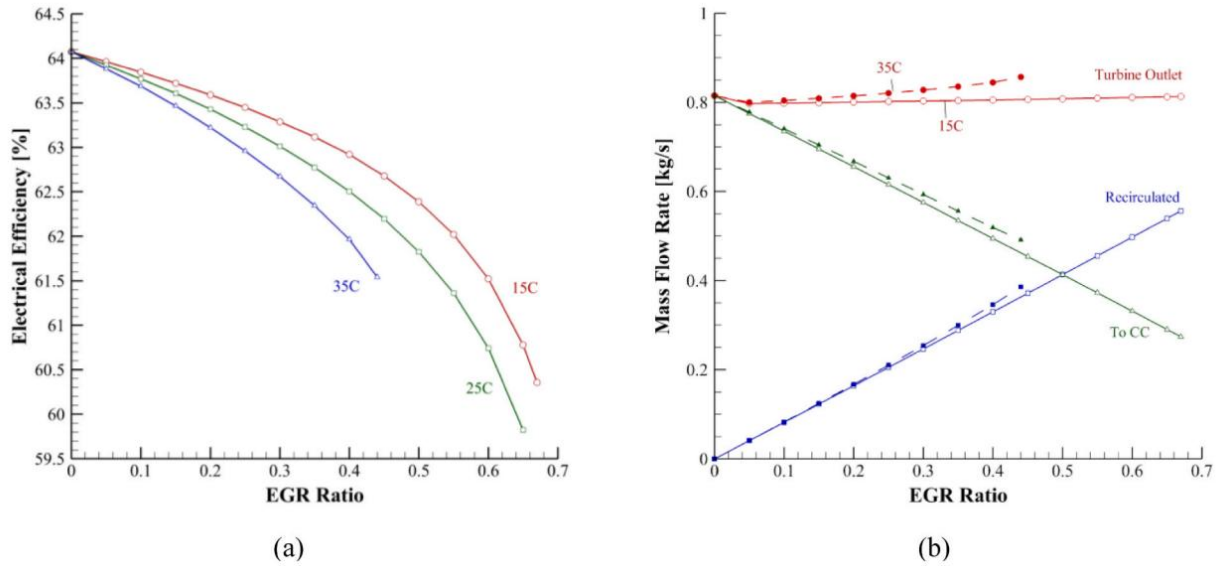

Fig. 14. Variation of (a) mGT+SOFC+EGR electrical efficiency and (b) mass flow rate of three streams as a function of the EGR ratio at different EGR cooling temperatures.

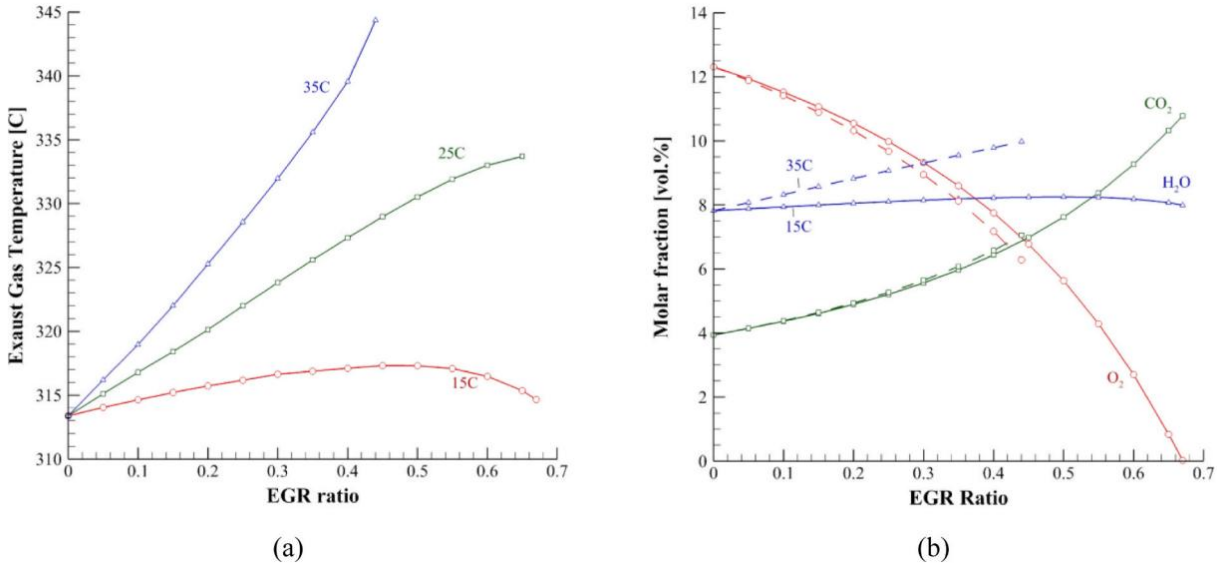

Fig. 15. Variation of (a) exhaust gas temperature and (b) molar fraction of three components in exhaust gas as a function of the EGR ratio at different EGR cooling temperatures.

by employing a direct-contact cooling tower, which enables reducing the EGR temperature below the ambient level through enhanced heat and mass transfer. When the EGR temperature increases to 25 ◦ C, there is a higher water vapor content in the gas phase, leading to a dilution effect and an additional reduction in the concentration of other species, including oxygen. Thus, the maximum permissible EGR ratio at this temperature is reduced to 0.65, beyond which the oxygen concentration is too low, and incomplete combustion will occur. At an even higher temperature of 35 ◦ C, the EGR limit is no longer oxygen shortage, as sufficient oxygen is still present for complete combustion; instead, compressor stability becomes the limiting factor. Increased EGR causes the density of the inlet stream to the compressor to decrease, and the operating point shifts towards the stonewall or stall region, where a trade-off exists between safe and stable compressor operation. Therefore, the maximum EGR ratio

at 35 ◦ C is found to be limiting at about 44%. To help describe and visualize these effects, the variations of operating conditions of the compressor are plotted on the compressor map in Fig. 16. The four red points on the map represent the operating points of the compressor at 0, 0.67 (15 ◦ C), 0.65 (25 ◦ C), and 0.44 (35 ◦ C) EGR ratios, respectively. As the EGR temperature rises, the operating point shifts toward higher pressure ratios and corrected mass flow rates, approaching the stonewall region. This indicates that at high temperatures, even modest EGR increases can push the compressor to its dynamic limits before oxygen deficiency occurs.

These effects can be better understood by noting that the mGT is designed to deliver a constant output of 100 kWe. Since the turbine outlet pressure is fixed and the turbine operates under choked conditions (with constant inlet temperature), an increase in fuel mass flow due to a higher EGR ratio necessitates a corresponding rise in inlet air mass flow. This, in turn, necessitates higher discharge pressure from the compressor, resulting in a higher compressor mass flow rate and pressure ratio, which eventually forces the compressor to the stonewall region. With rising recirculation temperatures, the lower density of the gas mixture increases this movement, and therefore the reason why the

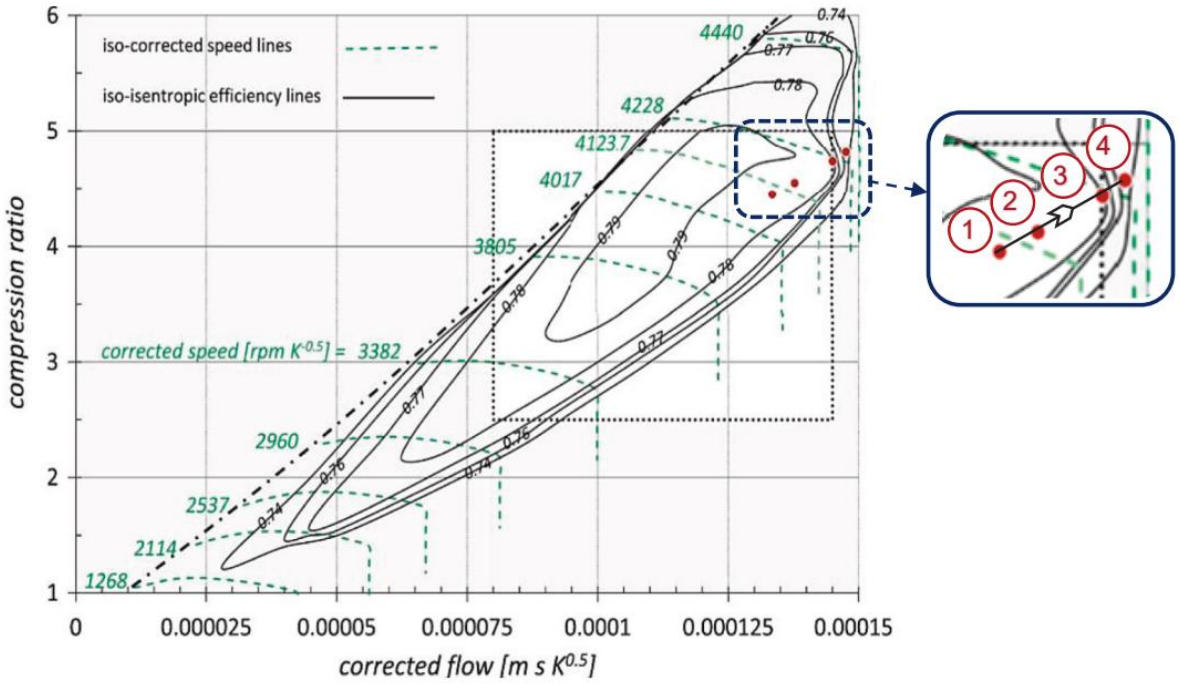

Fig. 16. Compressor map [42] showing the operating points under different EGR ratios and cooling temperatures, Point 1: without EGR, Point 2: EGR = 0.67, Point 3: EGR = 0.65, Point 4: EGR = 0.44.

compressor crosses its critical limit when the EGR stream is warmer at a lower EGR ratio.

Table 6 presents the key operating points previously defined as Points 1 to 4 in Fig. 16, corresponding to the base case without EGR and the maximum achievable EGR ratios at cooling temperatures of 15 ◦ C, 25 ◦ C, and 35 ◦ C. It highlights and compares the required active area, SOFC electrical power output, and SOFC efficiency (AC), providing a clear overview of the performance variations at these selected conditions. Although, as shown in this table, a lower EGR ratio results in higher efficiency, it should be noted that when the carbon capture unit is included, a lower EGR ratio leads to a higher energy penalty in the CO2 separation process.

Another technological issue in this hybrid system is the use of the EGR valve, which may increase the CO2 concentration in the air supplied the SOFC cathode. The presence of high CO2 concentrations is a significant concern because cathode catalysts tend to degrade more rapidly under these conditions. It has been demonstrated that the durability of certain cathode materials decreases when exposed to CO2 concentrations exceeding 5–10 vol% [43].

In addition to the previously mentioned technical constraints, a further limitation should be considered. The inherent fluctuations in the mass flow rate and composition of flare gas can lead to variations in SOFC power output, turbine inlet conditions, and overall system stability, requiring careful dynamic control to maintain safe and efficient operation.

Fig. 11 illustrates the thermodynamic characterization of the hybrid mGT + SOFC + EGR system at the design point, corresponding to an EGR ratio of 0.67 and a cooling temperature of 15 ◦ C. The system is

Table 6 Mgt + SOFC + EGR model simulation results.

Parameters	EGR (ratio, temperature)			
	withoutEGR	0.67,15 ◦ C	0.65,25 ◦ C	0.44,35 ◦ C
Required active area,[m2]	415.37	374.73	403.92	448
SOFC power output, DC[kW]	521.48	432.20	469.09	548.23
SOFC AC efficiency [LHV]	53.02%	48.71%	49.05%	51.68%

configured to maintain a net output of 100 kWe from the mGT, with the required SOFC power and other subsystem specifications determined accordingly.

3.4. Step 4. Carbon capture

In the final step, the exhaust gas leaving the hybrid mGT + SOFC + EGR system is routed to the downstream carbon capture. Due to the technical constraints previously identified for extensive EGR in the SOFC, two representative operating scenarios are considered: the first without EGR, and the second with an EGR ratio of 0.67 and a temperature of 15 ◦ C, which yields the highest CO2 concentration in the exhaust gas. The main thermodynamic properties of the exhaust gas under these conditions are summarised in Table 7.

After validating the pilot plant model, the carbon capture was scaled up for integration with the hybrid mGT + SOFC + EGR system. The column heights were selected based on the work of Giorgetti et al. [22], who employed columns for treating the exhaust gas from a Turbec T100 mGT with EGR. However, the column diameters were adjusted to prevent flooding. Throughout the simulations, a constant capture efficiency of 90% was applied, representing the typical CO2 removal rate in postcombustion capture processes. To ensure convergence of the model and achieve the targeted performance, several design specifications were introduced. The CO2 mass flow rate in the lean solvent was tuned to sustain the 90% absorption efficiency, while the reboiler duty in the stripper was adjusted to recover the exact amount of CO2 absorbed in the absorber. Additionally, the stripper reflux ratio was controlled to ensure a CO2 purity of 98 vol% in the captured stream.

The specifications of the absorber and stripper columns in the carbon

Table 7 Properties of the exhaust gas enters to CC.

Parameters	mGT + SOFC	mGT + SOFC + EGR
Mass flow rate [kg/s]	0.815	0.274
Temperature [◦ C]	313.39	314.67
Composition [vol.%]		
N2 [%]	75.93	81.201
CO2 [%]	3.94	10.783
H2O [%]	7.82	7.9894
O2 [%]	12.31	0.0264

capture unit are summarized in Table 8. The optimization of the conventional MEA process is carried out by examining the effects of solvent flow rate and stripper pressure on the reboiler duty, as presented below.

3.4.1. Effect of solvent flow rate

The liquid-to-gas ratio (*L/G*), defined as the ratio of liquid amine flow to gas mass flow at the absorber inlet, has a significant impact on the Specific Reboiler Duty (SRD), which is defined in Eq. (21):

$$SRD = \frac{\dot{Q}_{reboiler}}{\dot{m}_{CO_2}} \tag{21}$$

Excessively high or low liquid-to-gas ratios can lead to increased energy consumption for CO2 regeneration. At high *L/G* ratios, a larger volume of solvent must be heated, which raises the overall energy demand. Conversely, at low *L/G* ratios, although less solvent circulates, a higher CO2 cyclic capacity is required to maintain the desired capture rate (90%). This necessitates a significantly lower CO2 loading in the lean solvent, increasing the reboiler duty to preserve the driving force for desorption. Therefore, an optimal *L/G* ratio exists where the specific reboiler duty reaches a minimum. In the present study, the optimal liquid-to-gas ratio is found to be highly dependent on the exhaust gas characteristics. As illustrated in Fig. 17(a), under an operating condition with a stripper pressure of 1.2 bar and in the absence of EGR, the optimal *L/G* ratio is approximately 1.3 kg/kg. This condition corresponds to a specific reboiler duty of about 5.3 MJ/kgCO2. When the EGR ratio is increased to 0.67, as shown in Fig. 17(b), however, significant changes are observed. The optimal *L/G* ratio shifts to nearly 3.4 kg/kg, indicating that a higher solvent circulation rate is required to handle the modified exhaust gas composition. At the same time, the *SRD* increases slightly to around 5.65 MJ/kgCO2. Despite these variations in operating parameters, the reboiler temperature remains almost unchanged at approximately 107 ◦ C in both scenarios, as shown in Fig. 17.

3.4.2. Effect of stripper pressure

The effect of regeneration pressure variations was investigated by simulating different stripper pressure levels. An increase in stripper pressure leads to a decrease in regeneration energy. As illustrated in Fig. 17(a), for the case without EGR, when the stripper pressure rises from 1.2 to 1.8 bar, the optimal *SRD* decreases from 5.3 to 4.59 MJ/ kgCO2, corresponding to a reduction of 13.4%. In parallel, the optimal *L/ G* ratio decreases from 1.3 to 1.1 kg/kg. Similarly, as shown in Fig. 17 (b), for the case with EGR, increasing the stripper pressure from 1.2 to 1.8 bar reduces the optimal *SRD* from 5.65 to 4.67 MJ/kgCO2, corresponding to a reduction of 17.34%. In this case, the optimal *L/G* ratio decreases from 3.4 to 2.8 kg/kg.

Moreover, increasing the stripper pressure results in a higher reboiler temperature. For instance, as illustrated in Fig. 17(a), with an increase in pressure from 1.2 to 1.8 bar, the reboiler temperature at the optimal *L/G* point rises from 107.42 ◦ C to 119.32 ◦ C. However, elevated temperatures can accelerate amine degradation and cause corrosion problems. Therefore, when using 30 wt% MEA, the reboiler temperature should not exceed 125 ◦ C [44]. Therefore, a stripper pressure of 1.8 bar was selected for both cases, as it provides the optimal energy demand of the CC process.

Table 8 Carbon capture columns specifications.

Parameters	Without EGR	With EGR
Absorber height [m]	6	6
Absorber diameter [m]	0.7	0.4
Stripper height [m]	6	6
Stripper diameter [m]	0.3	0.3
Packing type	IMPT	
Packing size [mm]	38	
Absorber pressure [bar]	1.013	
Stripper pressure	1.2, 1.5, 1.8	

3.4.3. Effect of absorber height

In this section, after determining from the previous analysis that a stripper pressure of 1.8 bar provides the best performance for both cases (with and without EGR) at an absorber height of 6-m, the effect of absorber height on system performance is investigated. Accordingly, two additional absorber heights of 10 m and 14 m are examined to evaluate their influence on the *SRD* at different *L/G* ratios.

As shown in Fig. 18(a), in the case without EGR, increasing the absorber height from 6 m to 10 m leads to a reduction in the *SRD* values across all *L/G* ratios. The minimum SRD occurs at an *L/G* ratio of 1 for the 10 m absorber height, with a value of 4.27 MJ/kgCO2. This represents an approximate 6.88% reduction compared to the optimal *SRD* value obtained at the 6 m absorber height. However, with a further increase in absorber height to 14 m, only a slight reduction in *SRD* is observed. The minimum *SRD* reaches approximately 4.22 MJ/kgCO2 at an *L/G* ratio of 1, corresponding to only a 1.24% decrease compared to the value obtained at a 10 m absorber height. In Fig. 18(b), the same analysis is performed for the case with EGR. Similar to the previous case, increasing the absorber height to 10 m results in an *SRD* of 4.15 MJ/kgCO2, occurring at an *L/G* ratio of 2.6. This represents an 11.12% reduction compared to the 6 m absorber height. However, with a further increase in height to 14 m, the minimum *SRD* occurs at an *L/G* ratio of 2.4, reaching 3.99 MJ/kgCO2, which corresponds to a 3.86% decrease compared to the 10 m absorber height.

In Fig. 18, the reboiler temperature is plotted as a function of the *L/G* ratio at different absorber heights for both cases, with and without EGR. In both cases, increasing the *L/G* ratio and the absorber height exhibit a similar effect, as both lead to a reduction in the reboiler temperature. The minimum reboiler temperature occurs at the highest *L/G* ratio and an absorber height of 14 m, where the temperature is 116.51 ◦ C for the case without EGR and 116.83 ◦ C for the case with EGR.

In Fig. 19, the thermodynamic results of the streams in the carbon capture are illustrated for the optimal *L/G* value, optimal absorber height, and a stripper pressure of 1.8 bar, considering the case with an EGR ratio of 0.67. As shown, since the exhaust gases entering this unit from the previous stage have a relatively high temperature (314.67 ◦ C), their thermal energy can be utilized to partially supply the reboiler heat demand. As shown by the blue lines in the figure, water at a pressure of 3 bar is employed as the heat transfer medium, transferring energy from the hot exhaust gas to the reboiler. When passing through the heat recovery exchanger, the water absorbs a portion of the heat from the hot exhaust gases, with the pinch point set to 10 ◦ C. However, this heat is not sufficient to meet the energy demand of the reboiler. Therefore, an electric heater is installed to convert the water to saturated steam at that pressure (considering a 3% pressure drop in the heat recovery exchanger). The saturated steam then enters the reboiler, providing the necessary heat and condensing into saturated liquid. In the reboiler, a further 3% pressure drop is considered. The saturated liquid is then directed to a pump to overcome the pressure drops in this loop, and the cycle repeats. The use of saturated steam at the reboiler inlet and its condensation to saturated liquid at the outlet ensures a flat temperature profile along the reboiler, preventing sudden local temperature changes and the degradation of the solvent. It should be noted that in the case without EGR, due to the higher exhaust gas mass flow rate (as reported in Table 7), the entire reboiler heat requirement can be covered by the exhaust gas thermal energy, eliminating the need for the electric heater, while in the case with EGR, the electric heater provides 95.96 kW as shown in Fig. 19.

4. Overall performance analysis of the system

4.1. Energy analysis

After evaluating each subsystem, performing sensitivity analyses, and identifying the optimal operating points, it is now necessary to analyze the overall system from an energy perspective and calculate its

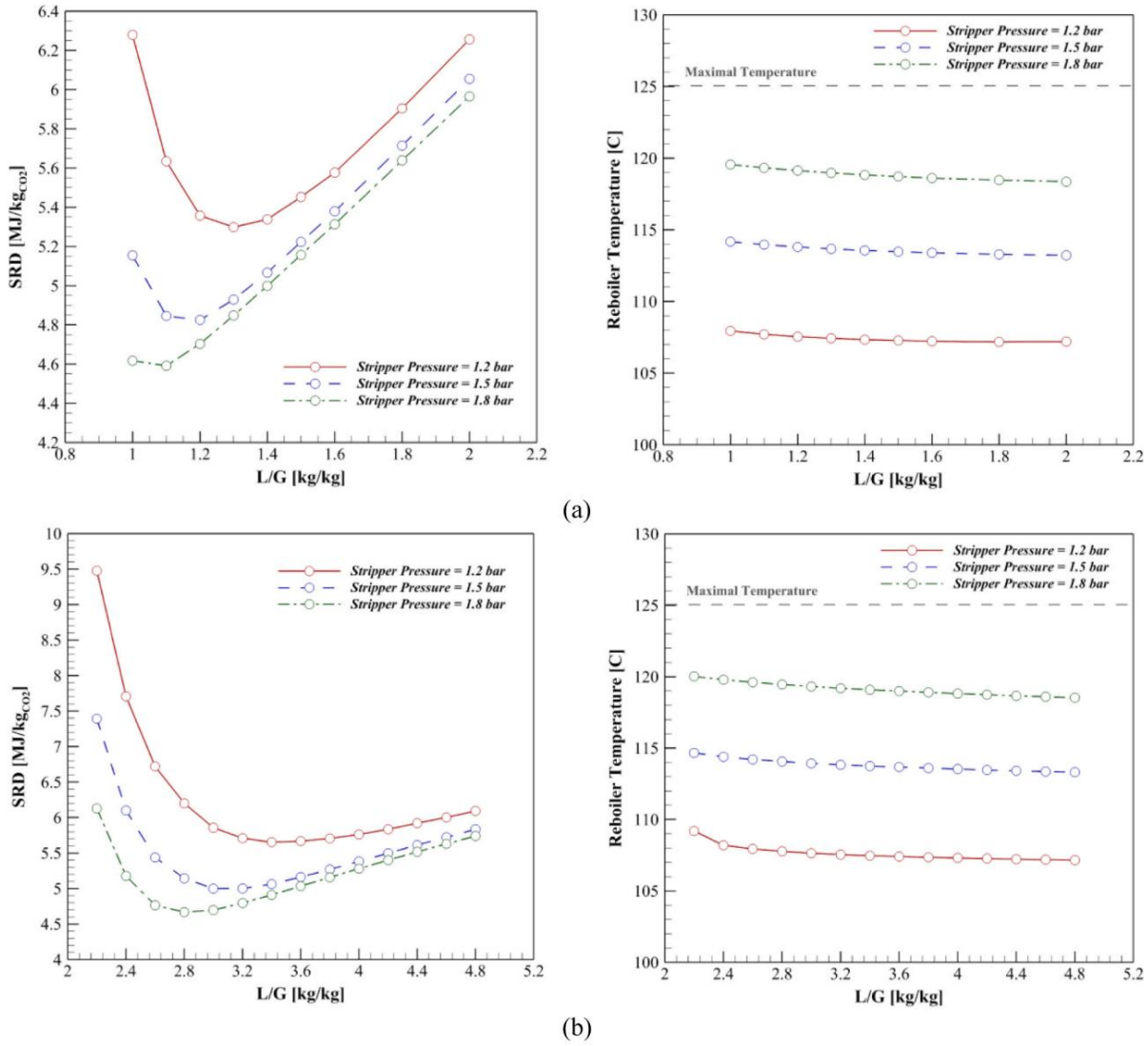

Fig. 17. The effect of liquid-to-gas ratio on specific reboiler duty and reboiler temperature in different stripper pressure for (a) without EGR, (b) EGR ratio = 0.67.

efficiency. Accordingly, the electrical efficiency is defined as follows:

$$\eta_{el} = \frac{\dot{W}_{el} - \dot{W}_{alix}}{\dot{m}_{sg}, LHV_{sg}} \tag{22}$$

where, $\dot{W}_{el}$ represents the electrical power output (DC) of the system (mGT + SOFC), while $\dot{W}_{aux}$ denotes the power required by auxiliary components such as pumps, the electric heater, and blowers. $\dot{m}_{sg}$ represents the mass flow rate of the sweet gas from the gas sweetening unit, and its lower heating value is denoted by LHV_{sg} . It should be noted that the gas sweetening unit is excluded from the electrical efficiency calculations. This is because, given the characteristics of the flare gas in the target field, the inlet flare gas flow rate to the sweetening unit is relatively high, and not all of the treated and sweet gas exiting this unit is intended to be directed to the hybrid mGT + SOFC system. Moreover, it is worth noting that, regardless of the specific application, the presence of a gas sweetening unit is always required.

4.2. Exergy analysis

For a more rigorous assessment, the system exergy efficiency should

also be evaluated. The exergy efficiency of the whole plant is defined as:

$$\eta_{ex} = \frac{\dot{E}x_{out}^{useful}}{\dot{E}x_{in}^{fuel}} \tag{23}$$

In the present work, since only net electrical power is considered as the useful output and no useful heat is exported, the numerator simplifies to the net electrical power.

$$\eta_{ex} = \frac{\dot{W}_{el} - \dot{W}_{aux}}{\dot{m}_{sg}, (ex_{ph,sg} + ex_{ch,sg})}$$

(24)

where, $ex_{ph.sg}$ and $ex_{ch.sg}$ are the specific physical and chemical exergy of the sweet gas [kJ/kg], respectively.

For a better comparison between different operating conditions of the system, the electrical power, electrical efficiency, and exergy efficiency of various system configurations are compared in Fig. 20. As previously noted, the system was analyzed at the design operating point, where the net electrical output of the mGT was fixed at 100 kW_e throughout all simulations.

Fig. 20(a) illustrates the electrical power output in different system

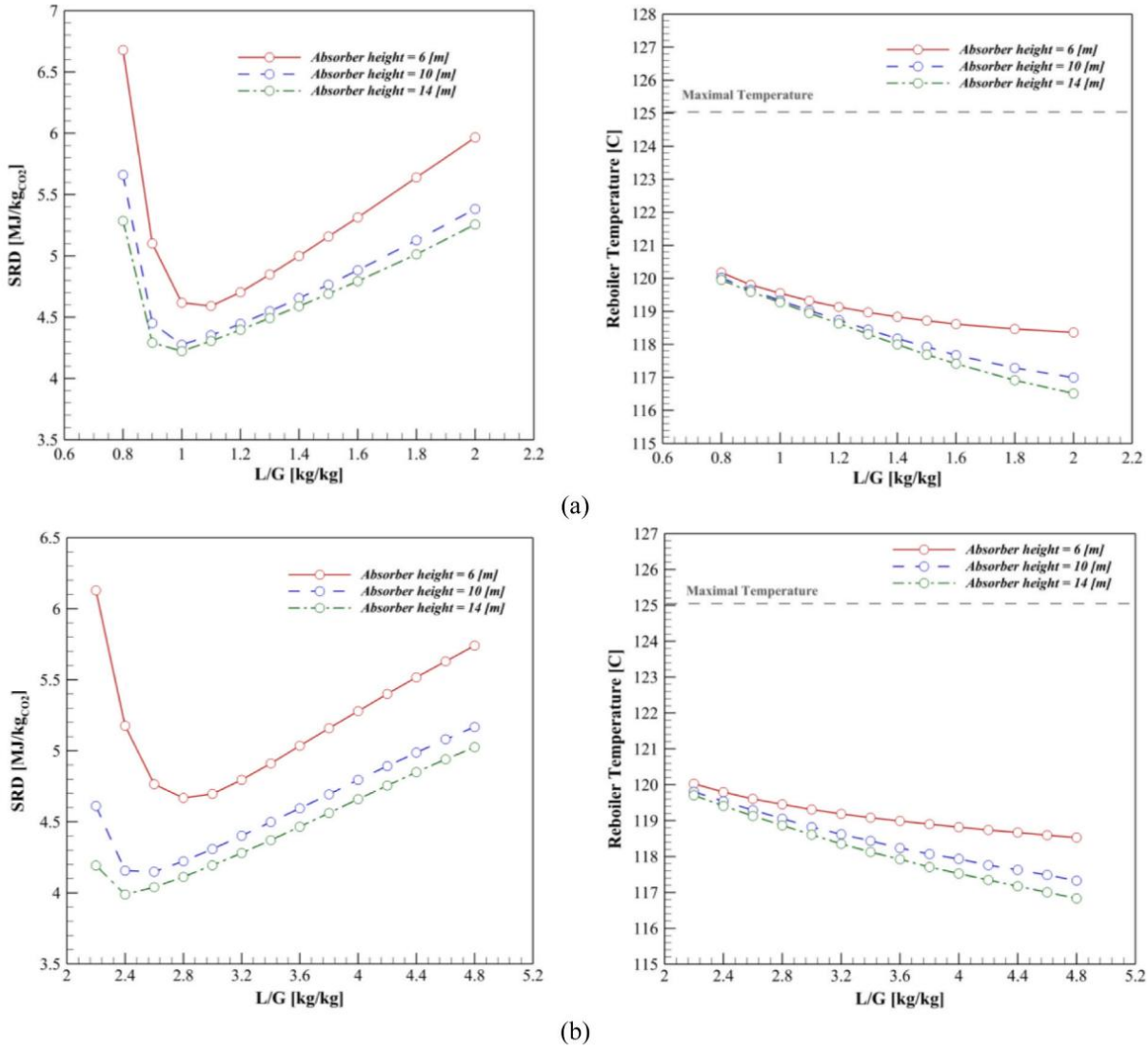

Fig. 18. The effect of liquid-to-gas ratio on specific reboiler duty and reboiler temperature in different absorber height for (a) without EGR, (b) EGR ratio = 0.67.

configurations. In the reference case [45], the standalone mGT generates about 100 kWe of power, while the integration of a SOFC significantly enhances the output to 621.48 kWe. The addition of an EGR valve to the mGT + SOFC configuration reduces the power to 527.28 kWe, whereas coupling the system with a CC maintains the output at 580.39 kWe. Finally, the simultaneous integration of SOFC, EGR, and CC with the mGT leads to a considerable decrease in power generation to 417.92 kWe.

Fig. 20(b) illustrates the electrical and exergy efficiencies for different system configurations. In the reference case, the standalone mGT shows relatively low efficiencies of 30% and 29.3%, respectively. With SOFC integration, these values rise sharply to 68.68% and 66.09%. Adding EGR slightly reduces the efficiencies to 64.59% and 62.15%, while coupling with CC gives similar values of 64.14% and 61.72%. In contrast, the combined mGT + SOFC + EGR + CC configuration results in a notable decline, with efficiencies dropping to 51.20% and 49.26%, respectively. Overall, SOFC integration provides the highest efficiency improvement, whereas EGR and especially its combination with CC diminish the system' s performance.

As presented in Table 9, although the reviewed studies [46–48], utilize different fuel types, including biomass, natural gas, and municipal sludge, they operate within a comparable power range and employ similar SOFC- and

gas turbine-based configurations with carbon capture. The proposed system achieves an electrical efficiency of 64.14%, which is higher than those reported in other studies. Similarly, the exergy efficiency of the present work reaches 61.72%, exceeding the corresponding values of 55.59% and 47.04% reported in Refs. [46] and [47], respectively. These results indicate that the hybrid mGT + SOFC + CC system enables more effective utilization of the fuel energy and exergy. Overall, the proposed configuration demonstrates competitive and favorable thermodynamic performance compared to similar systems, confirming the effectiveness of the system design.

4.3. Environmental analysis

Based on the simulated hybrid system operation, the carbon intensity of electricity generation (in gCO2/kWhe) is as follows. For the case without CC, the hybrid mGT + SOFC system has 288.46 gCO2/kWhe, and the mGT + SOFC + EGR system has 306.73 gCO2/kWhe. With carbon capture added to each configuration, the carbon intensities are reduced to 30.50 gCO2/kWhe (for the mGT + SOFC + CC) and 38.97 gCO2/kWhe (for the mGT + SOFC + EGR + CC). The reductions correspond to decreases of approximately 89.43% and 87.29%, respectively, versus their respective baselines without CC. All of the reported carbon intensity values were based on the net electrical power of the entire system in each configuration. Although the carbon intensity is slightly higher with

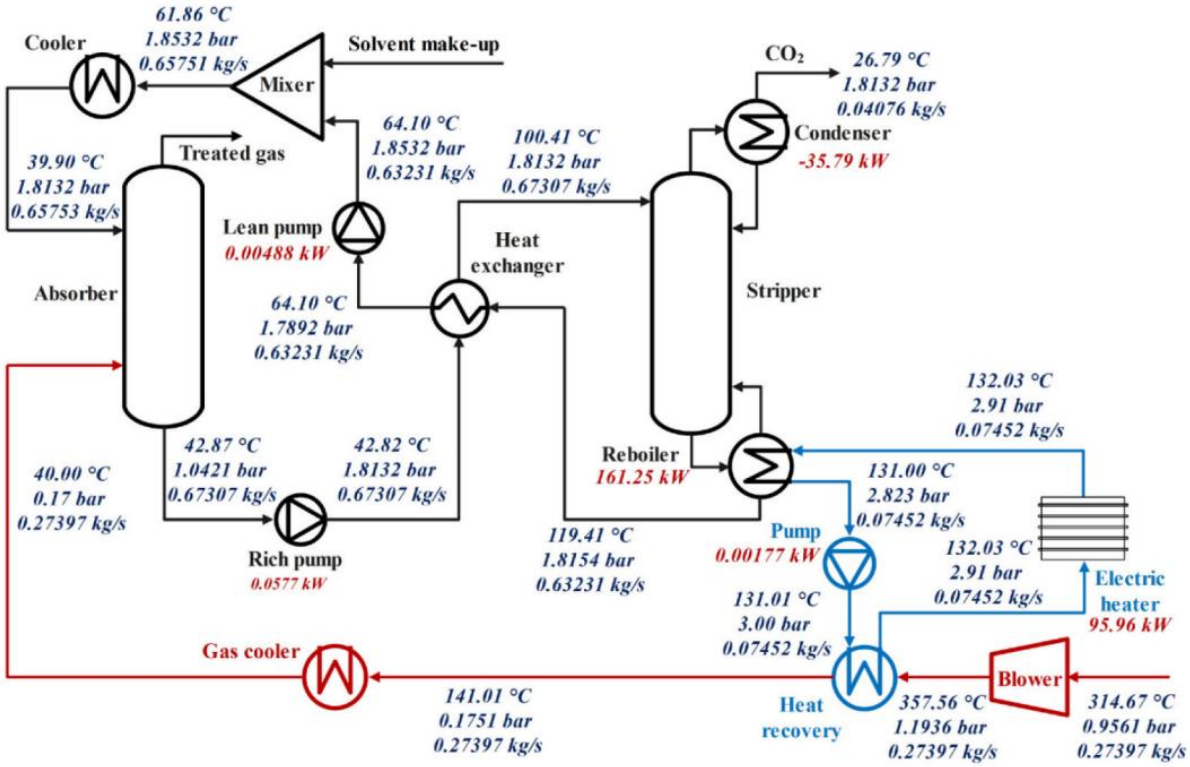

Fig. 19. Thermodynamic characteristics of the streams in CC (EGR ratio = 0.67, L/G = 2.4 [kg/kg], stripper pressure = 1.8 [bar], absorber height = 14 [m]).

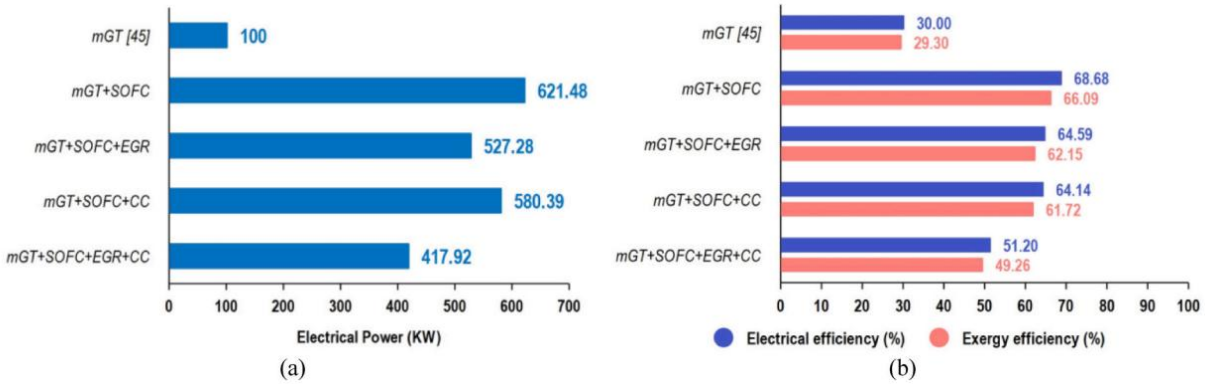

Fig. 20. Compression between different configuration based on (a) electrical power and (b) electrical and exergy efficiencies.

Table 9 Comparison of the present work with similar studies.

Reference	SystemDescription	Net PowerOutput(kW)	ElectricalEfficiency (%)	ExergyEfficiency(%)
Giorgetti etal [48]	mGT + EGR +CC	<100	21.4	–
Zhao et al.[46]	SOFC + CHPa+ CC	145.24	60.28	55.59
Zhang et al.[47]	SOFC + GT +SCBCb + CC	175.03	50.00	47.04
Presentwork	mGT + SOFC +CC	580.39	64.14	61.72

a Combined Heat and Power (CHP).

EGR, this configuration is retained because it allows for a reduction in the capital expenditure (CAPEX) required for the carbon capture unit, making the overall system economically more favorable.

4.4. Economic analysis

Although a comprehensive economic analysis is beyond the scope of this study, a preliminary estimation of the capital costs (CAPEX) for the subsystems is provided to assess the economic feasibility of the proposed configuration. The SOFC represents one of the main and most expensive components of the system. Based on similar studies [49,50], the capital cost of the SOFC and associated equipment is estimated to be approximately $395,000, indicating a significant share of the total system investment. Regarding electricity generation using a micro gas turbine, published economic data indicate that the capital investment of a ~ 100 kW mGT is approximately €23,000, which can be considered a reliable benchmark for estimating the cost of this component in the present system. A preliminary assessment of the carbon capture unit based on MEA is also presented. The capital cost of this unit primarily depends on the size of the columns and the gas flow rates. According to literature data [51], the CAPEX for MEA-based systems is within a reasonable range and is comparable to other carbon capture technologies.

Operational costs (OPEX) include electricity and heat consumption, solvent make-up, and maintenance. The reduction in usable heat from

b Supercritical CO2 Brayton Cycle (SCBC).

the micro gas turbine due to the carbon capture process is generally compensated by an auxiliary heat source, and the volatility of electricity prices introduces significant uncertainty in the OPEX estimation. Nevertheless, the use of MEA as a solvent is economically advantageous compared to other alternatives and does not represent a major portion of the total system cost.

5. Conclusion

In this study, a hybrid system comprising a flare gas sweetening unit, a solid oxide fuel cell, a micro gas turbine, and a carbon capture was investigated and simulated. The simulations were conducted using Aspen Plus, and all subsystems were initially modeled and validated independently.

The obtained results indicate:

- Packing height and lean solvent flow rate have a significant impact on H2S removal efficiency. A packing height of 30 m and a solvent flow rate of 0.29 kg/s yield the lowest reboiler duty and the most favorable operational conditions for producing sweet gas in compliance with industrial standards.
- Current density, steam-to-carbon ratio, and fuel utilization factor significantly impact cell voltage, power output, efficiency, and air and fuel flows. The optimal point at Uf = 0.85, Ic = 178 mA/cm2 , and S/C = 2.5 ensures balanced CO2 production for capture, high electrical efficiency, and prevention of fuel shortage. Operating at this point reduces fuel consumption and greenhouse gas emissions, improving the system' s environmental performance.
- Using EGR increases CO2 concentration in the exhaust, but excessive EGR can reduce total power output and cause compressor overpressure. The maximum allowable EGR ratio is 0.67 at 15 ◦ C, 0.65 at 25 ◦ C, and 0.44 at 35 ◦ C.
- The reboiler heat requirement is partially supplied by SOFC and mGT exhaust heat, reducing external energy demand and increasing thermal efficiency. The liquid-to-gas ratio and stripper pressure directly affect the specific reboiler duty and capture performance. At 1.8 bar, the optimal L/G ratio is 1.1 kg/kg without EGR and 2.8 kg/ kg with 0.67 EGR, resulting in a reboiler temperature around 119 ◦ C, ensuring thermal stability while minimizing energy consumption.
- The results show that increasing the absorber height leads to lower SRD and reboiler temperatures in both cases. At an absorber height of 14 m, the minimum SRD reaches 4.22 MJ/kgCO2 without EGR and 3.99 MJ/kgCO2 with EGR. The corresponding minimum reboiler temperatures are approximately 116.5 ◦ C and 116.8 ◦ C, respectively. Integrating SOFC with mGT provides the highest increase in power output and electrical (68.68%) and exergy (66.09%) efficiencies, while adding EGR and CC slightly reduces power and efficiency. The carbon capture unit decreases CO2 intensity by ∼ 89.5%, making mGT + SOFC the optimal configuration for energy performance and efficiency, with CC recommended to reduce environmental impact.

Overall, the proposed model accurately predicts the performance of the hybrid system, demonstrating that a hybrid mGT + SOFC system, when combined with proper management of recirculated flows, can optimize both energy efficiency and CO2 capture simultaneously. Enhanced electrical efficiency and use of recovered heat improve economic performance while reducing environmental impacts and greenhouse gas emissions, providing guidance for designing and optimizing similar hybrid energy systems in the energy and refinery industries.

CRediT authorship contribution statement

Mostafa Mahboobi: Writing –original draft, Visualization, Validation, Software, Methodology, Investigation, Formal analysis, Data curation, Conceptualization. **Antoine Verhaeghe:** Writing –review & editing, Validation. **Ward De Paepe:** Writing –review & editing, Validation, Supervision, Resources, Project administration, Methodology, Conceptualization.

Declaration of competing interest The authors declare that they have no known competing financial interests or personal relationships that could have appeared to influence the work reported in this paper.

Acknowledgments

The authors would like to thank the University of Kashan for facilitating the short-term exchange program conducted at the Thermal Engineering and Combustion Unit of the University of Mons. The authors also wish to thank the University of Mons for its valuable collaboration and hospitality during this research stay. Part of the research was performed within the Framework of the RESTORE project, Convention nr. 2410153 and nr. 2450340, CETP-2023-1 Research Programme.

Data availability

Data will be made available on request.

References

- [1] Soltanieh M, Zohrabian A, Gholipour MJ, Kalnay E. A review of global gas flaring and venting and impact on the environment: case study of Iran. Int J Greenh Gas Control 2016;49:488–509. https://doi.org/10.1016/j.ijggc.2016.02.010.
- [2] Asadi J, Yazdani E, Hosseinzadeh Dehaghani Y, Kazempoor P. Technical evaluation and optimization of a flare gas recovery system for improving energy efficiency and reducing emissions. Energy Convers Manag 2021;236:May. https://doi.org/ 10.1016/j.enconman.2021.114076.
- [3] About GFMR. Accessed: Sep. 27, 2025. [Online]. Available: https://www.worldba nk.org/en/programs/gasflaringreduct
- [4] Orisaremi KK, Chan FTS, Chung NSH. Potential reductions in global gas flaring for determining the optimal sizing of gas-to-wire (GTW) process: an inverse DEA approach. J Nat Gas Sci Eng 2021;93(September). https://doi.org/10.1016/j. jngse.2021.103995.
- [5] Tahmasebzadehbaie M, Sayyaadi H. Technoeconomical, environmental, and reliability assessment of different flare gas recovery technologies. J Clean Prod Sep. 2022;367. https://doi.org/10.1016/j.jclepro.2022.133009.
- [6] "New EU Methane Regulation to reduce harmful emissions from fossil fuels in Europe and abroad." Accessed: Nov. 11, 2025. [Online]. Available: https://energy. ec.europa.eu/news/new-eu-methane-regulation-reduce-harmful-emissions-fossilfuels-europe-and-abroad-2024-05-27_en.
- [7] A. Khalili-Garakani, M. Iravaninia, M. Nezhadfard, A review on the potentials of flare gas recovery applications in Iran, Jan. 10, 2021, Elsevier Ltd. doi: 10.1016/j. jclepro.2020.123345.
- [8] Khalili-Garakani A, Nezhadfard M, Iravaninia M. Enviro-economic investigation of various flare gas recovery and utilization technologies in upstream and downstream of oil and gas industries. J Clean Prod Apr. 2022;346. https://doi.org/ 10.1016/j.jclepro.2022.131218.
- [9] Al-Khori K, Bicer Y, Koç M. Integration of solid oxide fuel cells into oil and gas operations: needs, opportunities, and challenges. J Clean Prod Oct. 2019;245: 118924. https://doi.org/10.1016/j.jclepro.2019.118924.
- [10] Al-Khori K, Bicer Y, Aslam MI, Koç M. Flare emission reduction utilizing solid oxide fuel cells at a natural gas processing plant. Energy Rep Nov. 2021;7:5627–38. https://doi.org/10.1016/j.egyr.2021.08.164.
- [11] Saidi M, Siavashi F, Rahimpour MR. Application of solid oxide fuel cell for flare gas recovery as a new approach; a case study for Asalouyeh gas processing plant, Iran. J Nat Gas Sci Eng 2014;17:13–25. https://doi.org/10.1016/j.jngse.2013.12.005.
- [12] H. Al Jabri, N. Ahmed, A. Husain, A. Al-Janabi, Design of Solid Oxide Fuel Cell (SOFC) Model for Flare to Power Conversion, vol. 2040, pp. 620–629, 2025, doi: 10.46254/gc02.20240121.
- [13] Bargo MI. Recovery of flared natural gas with high CO2 content using SOFC CHP system: feasibility study for Neem-Field, Sudan. Int J Eng Res Africa 2023;67:1–15. https://doi.org/10.4028/p-E7ehFB.
- [14] Nezhadfard M, Khalili-Garakani A. Power generation as a useful option for flare gas recovery: enviro-economic evaluation of different scenarios. Energy Aug. 2020; 204. https://doi.org/10.1016/j.energy.2020.117940.
- [15] Farooqi AS, et al. Removal of carbon dioxide and hydrogen sulfide from natural gas using a hybrid solvent of monoethanolamine and N-methyl 2-pyrrolidone. ACS Omega Jun. 2024;9(24):25704–14. https://doi.org/10.1021/ ACSOMEGA.3C09100.
- [16] Jafari M, Spallina V, Ghasemzadeh K. Techno-economic assessment of flare gas valorisation during membrane-based GTL process by net-zero strategy. Energy Convers Manag 2024;315, no. June:118796. https://doi.org/10.1016/j. enconman.2024.118796.
- [17] Dinani AM, Nassaji A, Hamzehlouyan T. An optimized economic-environmental model for a proposed flare gas recovery system. Energy Rep 2023;9:2921–34. https://doi.org/10.1016/j.egyr.2023.01.103.

- [18] Kumar L, Sleiti AK, Al-Ammari WA, Hassan I, Rezaei-Gomari S, Rahman MA. Thermo-economic analysis of flare gas recovery for power and clean water production using integrated concentrated solar power and direct oxy-fuel combustion. Energy Oct. 2025;335:138091. https://doi.org/10.1016/J. ENERGY.2025.138091.
- [19] Zhang S, Nie X, Bi Y, Yan J, Liu S, Peng Y. Experimental study on NOx reduction of diesel engine by EGR coupled with SCR. ACS Omega 2024;9(7):8308–19. https:// doi.org/10.1021/acsomega.3c09052.
- [20] Thielens V, Demeyer F, Geigle KP, Kutne P, De Paepe W. Experimental investigation of the emissions and performance of a micro gas turbine setup with enhanced EGR. Appl Therm Eng 2024;267(September):2025. https://doi.org/ 10.1016/j.applthermaleng.2025.125673.
- [21] De Paepe W, Carrero MM, Giorgetti S, Parente A, Bram S, Contino F. Exhaust gas recirculation on humidified flexible micro gas turbines for carbon capture applications. Proc ASME Turbo Expo Sep. 2016;3. https://doi.org/10.1115/ GT2016-57265.
- [22] Giorgetti S, Bricteux L, Parente A, Blondeau J, Contino F, De Paepe W. Carbon capture on micro gas turbine cycles: assessment of the performance on dry and wet operations. Appl Energy Dec. 2017;207:243–53. https://doi.org/10.1016/J. APENERGY.2017.06.090.
- [23] Agbonghae EO, Best T, Finney KN, Palma CF, Hughes KJ, Pourkashanian M. Experimental and process modelling study of integration of a micro-turbine with an amine plant. Energy Procedia Jan. 2014;63:1064–73. https://doi.org/10.1016/ J.EGYPRO.2014.11.114.
- [24] Zhang Y, Que H, Chen CC. Thermodynamic modeling for CO2 absorption in aqueous MEA solution with electrolyte NRTL model. Fluid Phase Equilib Dec. 2011;311(1):67–75. https://doi.org/10.1016/J.FLUID.2011.08.025.
- [25] Baudoux A, Demeyer F, De Paepe W. Advanced configurations of amine based postcombustion carbon capture process applied to combined cycle gas turbine. Energy Convers Manag X 2024;22, no. February:100537. https://doi.org/10.1016/j. ecmx.2024.100537.
- [26] Snytnikov P, Potemkin D. Flare gas monetization and greener hydrogen production via combination with cryptocurrency mining and carbon dioxide capture. iScience 2022;25(2):103769. https://doi.org/10.1016/j.isci.2022.103769.
- [27] A. Verhaeghe, L. Dubois, L. Bricteux, D. Thomas, W. De Paepe, "Absorption-based carbon capture energy penalty reduction for low CO2 content applications: comparison of performance using different solvents and process configurations on micro gas turbine application," Energy, vol. 322, no. January, 2025, doi: 10.1016/ j.energy.2025.135505.
- [28] M. Qian, T. Xin, C. Xu, Y. Yang, A novel natural gas and coal hybrid power generation system for efficient utilization of gas turbine exhaust and low efficiency penalty of carbon capture, Appl. Therm. Eng., vol. 269, no. February, 2025, doi: 10.1016/j.applthermaleng.2025.126174.
- [29] K. Li, S. Zhang, Novel selective exhaust gas recirculation strategy for part-load performance of a gas turbine combined cycle with MEA-based CO2 capture, Energy Convers. Manag., vol. 346, no. June, 2025, doi: 10.1016/j. enconman.2025.120439.
- [30] Moosazadeh M, Ajori S, Taghikhani V, Moghanloo RG, Yoo CK. Sustainable hydrogen production from flare gas and produced water: a United States case study. Energy 2024;306, no. January:132435. https://doi.org/10.1016/j. energy.2024.132435.
- [31] Polasek J, Bullin J. Selecting amines for sweetening units. Energy Prog 1984;4(3): 146–50.
- [32] Gas Flare Smoke Petrochemical Refinery Environmental Stock Photo 2036683877 | Shutterstock. Accessed: Oct. 12, 2025. [Online]. Available: https://www.shutters tock.com/image-photo/gas-flare-smoke-petrochemical-refinery-environmental-2 036683877.
- [33] Zhang W, Croiset E, Douglas PL, Fowler MW, Entchev E. Simulation of a tubular solid oxide fuel cell stack using AspenPlusTM unit operation models. Energy
- Convers Manag 2005;46(2):181–96. https://doi.org/10.1016/j. enconman.2004.03.002.

- [34] Spallina V, Romano MC, Campanari S, Lozza G. A SOFC-based integrated gasification fuel cell cycle with CO2 capture. Proc ASME Turbo Expo Dec. 2010;3: 683–93. https://doi.org/10.1115/GT2010-22814.
- [35] F. Edition, W. Virginia, Fuel cell handbook, Choice Rev. Online, vol. 26, no. 11, pp. 26-6292-26–6292, 1989, doi: 10.5860/choice.26-6292.
- [36] Rochelle GT. Amine Scrubbing for CO2 Capture. Science (80- 2009;), 325(5948): 1652–4. https://doi.org/10.1126/science.1176731.
- [37] Boot-Handford ME, et al. Carbon capture and storage update. Energy Environ Sci 2014;7(1):130–89. https://doi.org/10.1039/c3ee42350f.
- [38] UKCCSRC Carbon Capture & Storage (CCS) UK CCS Research Centre (UKCCSRC) –PACT facilities - UKCCSRC. Accessed: Sep. 19, 2025. [Online]. Available: https ://ukccsrc.ac.uk/project_grant/uk-ccs-research-centre-ukccsrc-pact-facilities/.
- [39] Zhang Y, Chen H, Chen CC, Plaza JM, Dugas R, Rochelle GT. Rate-based process modeling study of CO2 capture with aqueous monoethanolamine solution. Ind Eng Chem Res Oct. 2009;48(20):9233–46. https://doi.org/10.1021/IE900068K.
- [40] Mouhoubi S, Dubois L, Loldrup Fosbøl P, De Weireld G, Thomas D. Thermodynamic modeling of CO2 absorption in aqueous solutions of N, Ndiethylethanolamine (DEEA) and N-methyl-1,3-propanediamine (MAPA) and their mixtures for carbon capture process simulation. Chem. Eng. Res. Des. 2020;158: 46–63. https://doi.org/10.1016/J.CHERD.2020.02.029.
- [41] Hanley B, Chen CC. New mass-transfer correlations for packed towers. AIChE J 2012;58(1):132–52. https://doi.org/10.1002/AIC.12574.
- [42] De Paepe W, Renzi M, Carrerro MM, Caligiuri C, Contino F. Micro gas turbine cycle humidification for increased flexibility: numerical and experimental validation of different steam injection models. J Eng Gas Turbines Power 2019;141(2):1–13. https://doi.org/10.1115/1.4040859.
- [43] Yang T, et al. Evaluation of the CO2 tolerant cathode for solid oxide fuel cells: Praseodymium oxysulfates/Ba0.5Sr0.5Co0.8Fe0.2O3-δ. Appl Surf Sci 2019;472: 10–5. https://doi.org/10.1016/j.apsusc.2018.07.174.
- [44] Biliyok C, Yeung H. Evaluation of natural gas combined cycle power plant for postcombustion CO2 capture integration. Int J Greenh Gas Control Nov. 2013;19: 396–405. https://doi.org/10.1016/J.IJGGC.2013.10.003.
- [45] Montero Carrero M, De Paepe W, Bram S, Parente A, Contino F. Does humidification improve the micro Gas Turbine cycle? Thermodynamic assessment based on Sankey and Grassmann diagrams. Appl Energy 2017;204:1163–71. https://doi.org/10.1016/j.apenergy.2017.05.067.
- [46] Zhao H, Lu R, Zhang T. Thermodynamic and economic performance study of SOFC combined cycle system using biomass and LNG coupled with CO2 recovery. Energy Convers Manag 2023;280(November). https://doi.org/10.1016/j. enconman.2023.116817.
- [47] Zhang J, et al. Thermodynamic analysis of SOFC–CCHP system based on municipal sludge plasma gasification with carbon capture. Appl Energy 2023;336 (September). https://doi.org/10.1016/j.apenergy.2023.120822.
- [48] Giorgetti S, Parente A, Bricteux L, Contino F, De Paepe W. Carbon clean combined heat and power production from micro gas turbines: thermodynamic analysis of different scenarios. Energy Procedia 2017;142:1622–8. https://doi.org/10.1016/j. egypro.2017.12.540.
- [49] Hentati M, Boussetta A, Elleuch A, Halouani K. Technical, environmental and economic evaluation of a kW-level flared gas-fuel GT-SOFC hybrid system. Energy Convers Manag 2024;317, no. July:118825. https://doi.org/10.1016/j. enconman.2024.118825.
- [50] A. H. Samitha Weerakoon, M. Assadi, Techno economic analysis and performance based ranking of 3–200 kW fuel flexible micro gas turbines running on 100% hydrogen, hydrogen fuel blends, and natural gas, J. Clean. Prod., vol. 477, no. June, 2024, doi: 10.1016/j.jclepro.2024.143819.

- [51] L. Dubois, A. Costa, S. Mouhoubi, G. De Weireld, D. Thomas, "Post-combustion CO2 capture process by absorption-regeneration applied to cement plant flue gases: techno-economic comparison between the use of a demixing solvent technology and an advanced process configuration," SSRN Electron. J., vol. 32, no. October, 2022, doi: 10.2139/ssrn.4271986.